



# RESEARCH MEMORANDUM

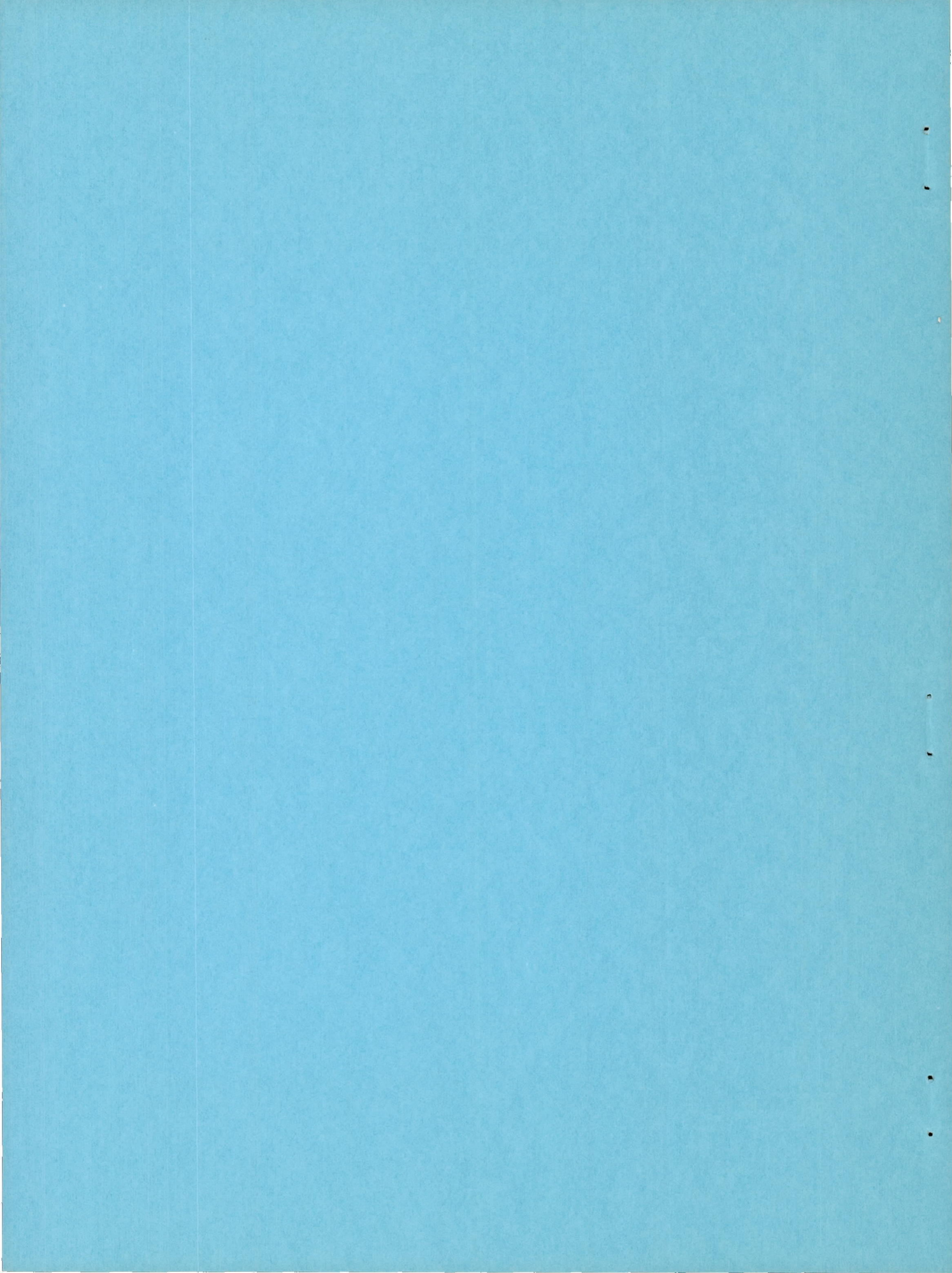
FLIGHT DETERMINATION OF THE PRESSURE RECOVERY AND DRAG  
CHARACTERISTICS OF A TWIN SIDE-INLET  
MODEL AT TRANSONIC SPEEDS

By Howard S. Carter and Charles F. Merlet

Langley Aeronautical Laboratory  
Langley Field, Va.

NATIONAL ADVISORY COMMITTEE  
FOR AERONAUTICS  
WASHINGTON

July 30, 1953  
Declassified May 8, 1957



## NATIONAL ADVISORY COMMITTEE FOR AERONAUTICS

## RESEARCH MEMORANDUM

---

FLIGHT DETERMINATION OF THE PRESSURE RECOVERY AND DRAG  
CHARACTERISTICS OF A TWIN SIDE-INLET  
MODEL AT TRANSONIC SPEEDS

By Howard S. Carter and Charles F. Merlet

## SUMMARY

Free-flight and free-jet tests of a twin side-inlet configuration, including a pilot's canopy and a wheel-well fairing, were made between Mach numbers of 0.8 and 1.55. Oscillating flow was encountered throughout the Mach number range. The maximum mass-flow ratio at which this oscillating flow occurred varied from approximately 0.63 at a free-stream Mach number of 0.80 to about 0.81 at a free-stream Mach number of 1.45. The total-drag coefficient was affected by the oscillating flow as much as  $\pm 0.10$  at Mach numbers greater than 1.1 and as much as  $\pm 0.09$  at Mach numbers less than 0.9.

At supersonic speeds, the minimum external-drag coefficient occurring at mass-flow ratios of 0.8 and 0.9 was about 0.35, a value considerably higher than that obtained with a body of revolution of the same fineness ratio. Throughout the Mach number range, the increase in external-drag coefficient with decreasing mass-flow ratio did not exceed 0.01 in the region of steady flow.

The maximum total-pressure recovery varied from 0.92 at a Mach number of 0.8 to 0.77 at a Mach number of 1.45. This latter value is about 18 percent less than the free-stream normal-shock recovery. Two alternate nose shapes, tested only at a Mach number of 1.55, yielded lower pressure recovery than the original nose. Total-pressure surveys made at the inlet at a Mach number of 1.55 indicated the presence of a thick boundary layer and, in some cases, separated flow at the inlet for all three nose shapes at all mass-flow ratios tested.

## INTRODUCTION

The use of a side inlet offers at least two important advantages to the aircraft designer: the inlet can be located closer to the engine,

thereby reducing the volume needed for internal ducting; and the nose is left available for other uses, such as radar or armament installations. Balanced against these advantages is the important problem of the effect of the boundary layer on the performance of the inlet. This problem becomes especially critical at transonic and supersonic speeds, when boundary-layer shock interaction may affect the behavior of the boundary layer. The severity of these effects largely determines the final merit of a particular side-inlet configuration.

Herein are presented the results of a pressure-recovery and drag investigation of a side-inlet configuration which encountered this boundary-layer problem. The particular configuration tested was designed for use on a transonic fighter-type aircraft. Twin side inlets were formed from an annular inlet by adding a pilot's canopy and a wheel-well fairing. The resulting inlets enclosed about one-half of the forebody circumference and had an inlet area equal to 15 percent of the maximum body frontal area. No provision was made for boundary-layer removal.

A rocket-propelled free-flight model was used to obtain the drag and pressure-recovery characteristics of the present side-inlet configuration through the transonic Mach number range. Because the number of channels of telemetering available for a flight test was limited, supplementary preflight tests of the flight model were conducted to aid in the reduction of the flight-test data. The testing technique, including the use of supplementary preflight tests, was the same as that reported in reference 1 and is more fully explained therein.

Also included in the preflight tests was an investigation to determine the effect of two alternate nose shapes on the total-pressure recovery of the configuration. This paper presents the results obtained from the flight and preflight tests.

#### SYMBOLS

A cross-sectional area, sq ft

$C_{D_{ext}}$  external-drag coefficient,  $\frac{D_T - D_i}{qS}$

$D_i$  internal drag,  $m(V_o - V_e) + (p_o - p_e)A_e$ , lb

$D_T$  total drag, lb

F force, lb

|       |   |
|-------|---|
| H     | total pressure, lb/sq ft  |
| L     | total length of model, ft   |
| m     | mass flow through the model   |
| $m_o$ | mass flow through a free-stream tube of the same area as the inlet, 12.6 sq in. |
| M     | Mach number   |
| p     | static pressure, lb/sq ft   |
| q     | dynamic pressure, lb/sq ft  |
| R     | Reynolds number per foot  |
| S     | body maximum frontal area, sq ft  |
| V     | velocity of the flow, ft/sec  |
| w     | distance across the inlet measured from lip inner wall, in.<br>(see fig. 3)     |
| W     | depth of inlet at a rake, in. (see fig. 3)                                      |
| X     | model station (see table I)   |

## Subscripts:

|   |                            |
|---|----------------------------|
| e | model exit                 |
| l | inlet minimum-area station |
| n | nose tip                   |
| o | free stream                |
| t | throat station             |
| x | longitudinal               |
| y | transverse                 |

## MODEL

A photograph of the model is presented in figure 1, and a drawing is shown in figure 2. Nose A, indicated in figure 2, was used for the flight test, whereas noses A, B, and C were tested in the preflight jet. Nose A had a fineness ratio of 3.1 and approximately a parabolic profile. Nose B had a larger apex angle and was shorter with a fineness ratio of about 2.5. Nose C was blunt and had a fineness ratio of about 2.3. All three noses were bodies of revolution and were identical from the beginning of the pilot's canopy to the inlet (station 12.64 to station 21.02, respectively). The coordinates are given in table I. The coordinates of the pilot's canopy and the wheel-well fairing are given in table II. The cross-sectional shape of the body just rearward of the inlets, exclusive of the pilot's canopy, was formed by joining two semielliptical sections, fairing into a circular exit. The coordinates of the body are given in table III.

The two inlets, located 21.5 inches from the tip of nose A, had a total inlet area of 12.6 square inches, measured on a plane perpendicular to the model center line and defined by the leading edge of the lips and the centerbody. No provision was made to remove the boundary layer. The rounded lips produced an inlet minimum-area station about 0.2 inch downstream of the inlet, with a contraction ratio of 0.92, based on total inlet area. Figure 3 shows a cross-sectional view of the model at the inlet minimum-area station, and table IV presents the lip coordinates.

Downstream of the inlet minimum-area station, a subsonic diffuser of 4.9 to 1 area ratio was used. The large area ratio was selected to facilitate flight measurements by providing a uniform total-pressure profile at the throat. The diffuser was designed according to the criterion of reference 2. This criterion states that the total-pressure losses of an annular diffuser are equal to the total-pressure losses of a conical diffuser having the same rate of change of diffuser surface area with cross-sectional area. Variation of surface area with cross-sectional area along the diffuser is presented in figure 4. After a 4-inch section of area ratio of 1.1 to 1, the rate of change of diffuser surface area with cross-sectional area was 21.4, which is the same value as that for a  $5.3^\circ$  total angle conical diffuser. The equivalent conical diffuser (that is, that conical diffuser that would give the same area ratio for the same length (4.9 to 1 in 29.8 in.) would have a total cone angle of  $6.4^\circ$ .

Transition was made from the circular diffuser section to a rectangular throat with an area 1.06 times the inlet area (fig. 5). A duct splitter installed along the diffuser and past the throat station kept the flow in the two ducts separate. Behind the throat station, the two

ducts were joined in a region of high velocity in order to reduce the tendency toward twin-duct instability, as suggested in reference 3.

The air flow was regulated by four shutters installed downstream of the splitter. The shutters were rotated during the tests by an electric motor. Downstream of the shutters, the duct made a transition to a round area of 1.6 times the total inlet area and was cylindrical to the exit.

The nose, innerbody, inlet lips, duct splitter, and all internal ducting were made of magnesium. The canopy, wheel well, and all of the model exterior back of the inlet lips were made of mahogany. The model was stabilized by four  $60^{\circ}$  half-delta fins of NACA 65A004 airfoil section. The total exposed fin area was 3.7 square feet.

## INSTRUMENTATION AND TESTS

### Flight Tests

A pressure tube installed in the nose measured pitot-stagnation pressure. Total pressure at the throat station was measured by two manifolds total-pressure tubes, located one on each side of the splitter in the center of the duct (fig. 2). The throat total pressure was referenced to the pitot stagnation pressure at the tip of the nose. Four wall-type static orifices, two in each duct (fig. 5), were manifolded together to measure an average static pressure at the throat. The throat static pressures were referenced to the throat total pressure. Static pressure at the exit was measured with four manifolds wall-type static-pressure orifices equally spaced circumferentially around the inner wall about 1 inch from the after end of the model. Side force was measured with a transverse accelerometer located within the canopy about 4 inches rearward of the inlet station, and total drag was measured with a longitudinal accelerometer located within the centerbody at the inlet station. A six-channel telemeter transmitted all of the data to ground receiving stations where continuous time histories were recorded on an oscillograph.

Velocity determined from CW Doppler radar was corrected for winds, as determined from radar observations of the radiosonde balloon released immediately after the flight test. Ambient air conditions were determined from radiosonde observations. Altitude was computed from the flight path determined by an NACA modified SCR 584 tracking radar.

The model was launched at  $60^{\circ}$  elevation angle and accelerated to maximum speed by a Deacon booster rocket. After burnout of the rocket motor, drag separation of the booster from the model occurred. All data

were obtained during the ensuing period of coasting flight, while the model decelerated to subsonic speeds. The air-flow regulation shutters turned continuously during the flight, taking approximately 0.4 second to vary the air flow from maximum to minimum. The Reynolds number per foot for the flight test is shown in figure 6 as a function of Mach number. The test was made at the Langley Pilotless Aircraft Research Station at Wallops Island, Va.

#### Preflight Tests

Ground tests were made in the preflight jet of the Langley Pilotless Aircraft Research Station at Wallops Island, Va. (ref. 4). A 27-inch-square, Mach number 1.55 nozzle was used. Tests were not conducted at a lower supersonic Mach number because at  $M < 1.55$  shock reflections from the jet boundaries would intersect the model ahead of the inlets. Each test was begun with the air-flow regulation shutters in position to give maximum flow. The test was continued until the shutters had rotated  $90^\circ$  to give minimum flow, a period of approximately 13 seconds. Previous tests had shown this rotation speed to be slow enough to yield steady-state results.

Total pressure at the right-inlet minimum-area station was measured with twelve 0.09-inch-outside-diameter total-pressure tubes flattened at the forward end (fig. 3). They were arranged in three rakes of four tubes each. Static pressure was measured at the same station with an innerbody wall orifice. Two total-pressure tubes and one static-pressure orifice, located at the same station (fig. 3), were used in the left-inlet duct.

Twenty 0.09-inch outside-diameter total-pressure tubes were installed in the left duct at the throat station (fig. 5). Static pressure at the same station was measured in each duct by two wall orifices manifolded together. In addition, the left duct had two static-pressure probes located on the rakes.

The free-jet total pressure, static pressure at free-jet nozzle exit, and stagnation pressure at the tip of each nose were also measured. Pressures were recorded by mechanical optical pressure recorders and electrical pressure recorders of the strain-gage type. Time histories were obtained on film. Shadowgraphs were taken of all tests.

A subsonic test at  $M_0 \approx 0.7$  was also made with the supersonic nozzle. This Mach number was obtained by decreasing the reservoir total pressure until the normal shock moved inside the nozzle and upstream of the model. A static-pressure survey along the nozzle determined the position of the normal shock. The pressure measured by the tube located at the nose tip of the model was used as free-stream stagnation pressure.

The model was at 0° angle of attack and yaw throughout all ground tests. The Reynolds numbers for these tests are also shown in figure 6.

#### METHOD OF ANALYSIS

The telemeter records obtained during the flight test indicated that oscillating flow occurred over a considerable portion of the mass-flow range tested. Some samples of the telemeter record are shown in figure 7. The use of manifolded tubes having different lengths of tubing between the measuring point and the instrument precluded the possibility of determining the actual amplitude or phase relationships of the various measured pressures.

The accelerometers, however, indicated the actual amplitude of forces encountered (figs. 7(c) and (d)). The measured amplitudes were corrected by multiplying by the amplitude factors for the instruments and the recorder used. The amplitude factors for a 60-cycle oscillation were 1.13 and 1.06 for the longitudinal and transverse accelerometers, respectively, while that of the recorder was 0.975. The square wave pulse was imposed on the nose stagnation-pressure channel  $H_n$  to indicate the point of minimum flow rate.

In the region of oscillating flow, curves were faired approximately through the midpoint of the oscillating traces, as shown in figure 7. These averages, instead of instantaneous values, were read and then reduced in the same manner as the nonoscillating flow data. Data obtained under oscillating flow conditions are presented as dashed curves on all figures.

External drag is defined herein as the summation of the dragwise components of all the pressure and viscous forces on the external body surface and the entering stream tube surface, except those forces which are common to both surfaces. The external drag was obtained by subtracting the internal drag from the total drag determined from the longitudinal accelerometer. The method used in computing internal drag from the measured pressures is explained in reference 1. The maximum value of internal-drag coefficient was approximately 0.09 and occurred at maximum mass-flow ratio. Mass-flow ratio and total-pressure recovery were computed from the total- and static-pressure measurements made at the throat station.

Because of the relatively high rotation speed of the shutters during the flight test, transient terms caused by the time rate of change of velocity within the duct appeared in the measured data. At maximum mass flows, however, the time rate of change was zero, and it was small for

mass flows near minimum. At intermediate mass flows, the transient terms were a maximum. The magnitude of these terms did not exceed the experimental accuracy. The method used to reduce these transient terms to negligible quantities to obtain equivalent steady-state conditions is discussed in reference 1.

In the preflight tests at  $M_\infty = 1.55$ , choking at the supports of the throat rakes limited the maximum mass-flow ratio attainable to a value of 0.79, and approximately 60-cycle oscillations were experienced throughout the mass-flow range tested for all three nose shapes. The instrumentation setup precluded accurate determination of instantaneous values or actual amplitude. Therefore, the average value of pressure was used for all tubes. The total-pressure profile at the throat station, obtained from these average values, was essentially uniform, and an arithmetic mean of the 20-tube readings was taken as the average total pressure  $H_t$ . The three static-pressure measurements in the left duct agreed within 2 percent and the arithmetic mean was used as the throat static pressure  $p_t$ . Mass-flow ratio and total-pressure recovery were then obtained from the average values of  $H_t$  and  $p_t$ .

## RESULTS AND DISCUSSION

In the following discussion, the results of the preflight and flight tests are presented together as they apply to the topic being discussed. Since the flight records indicated an oscillating flow over the major portion of the mass-flow range tested at all Mach numbers, the effects of this oscillating flow are discussed first. Then the values of external-drag coefficient and pressure recovery are presented for both the steady and oscillating flow cases. In general, the results of the preflight tests are used to support conclusions reached on the basis of flight-test data.

### Effects of Oscillating Flow

Figure 7 presents portions of the flight telemeter records showing pressure and force oscillations at supersonic and subsonic Mach numbers. Each portion of the records covers a period of time slightly longer than the mass-flow cycle. The approximately steady traces at each end of the records represent steady flow at high mass-flow ratios, whereas the oscillating traces toward the center of the records represent oscillating flow at reduced mass-flow ratios. The frequency of the oscillations varied from about 62 cycles per second at  $M_\infty = 1.4$  to 58 cycles per second at  $M_\infty = 0.8$ . Figure 7(a) shows that strong pressure oscillations

existed at supersonic speeds, and figure 7(b) shows that both strong and weak oscillations occurred at subsonic speeds. Figures 7(c) and 7(d) show the corresponding force oscillations at supersonic and subsonic speeds, respectively. Figure 8 shows the regions of oscillating flow as a function of Mach number and mass-flow ratio.

The longitudinal accelerometer data indicated that the strong oscillations had an amplitude that amounted to an increment in total-drag coefficient of about  $\pm 0.10$ . The transverse accelerometer data showed that the mean angle of yaw varied, not exceeding an angle of approximately  $0.8^\circ$ . Superimposed on this mean angle-of-yaw variation were the 60-cycle oscillations in side force. These high-speed oscillations had a maximum force amplitude corresponding to an angle of yaw of  $\pm 0.1^\circ$ . The angles of yaw were computed by determining the angle of yaw necessary for the fins to produce a side force equal to that measured by the transverse accelerometer.

The preflight-jet tests at  $M_0 = 1.55$  indicated that the oscillations were a result of unsteady flow ahead of the inlet. Shadowgraph pictures showed that the flow pattern ranged from that with a strong shock just ahead of the inlet lips to separated flow at the inlet with the point of separation on the nose, occurring as much as seven inlet heights upstream of the inlet. Reference 5 reports a similar phenomenon occurring on a sharp-lipped annular inlet having an innerbody with a fineness ratio of 2.5 over a Mach number range of 1.36 to 2.01. It is reasoned in reference 5 that separation was caused by the adverse pressure gradient which occurred in the region of the inlet as mass flow was reduced. Separation eliminated the adverse pressure gradient, allowing the flow to reattach, and the cycle was repeated. It is felt that the strong oscillations occurring at supersonic speeds during these tests were the result of a similar phenomenon. Furthermore, since some stable flow was obtained, it can be reasoned that the principal effect of the canopy and wheel-well fairing was to alter the range of stability.

At subsonic speeds, there appeared to be two types of oscillations - weak and strong. The weak oscillations appeared as small disturbances on the duct pressures and on the transverse accelerometer (fig. 7). These oscillations could have been a result of twin-duct instability. As discussed in reference 3, the point of peak static-pressure recovery is the point at which twin-duct instability may begin. Plotting the static-pressure recovery at the throat as a function of mass-flow ratio for the stable flow range indicated that the peak static-pressure recovery apparently occurred at  $m/m_0 \approx 0.6$ . This mass-flow ratio agrees quite well with the measured value of mass-flow ratio at which instability began (fig. 8).

At  $M < 0.9$ , the strong flow oscillations (fig. 8) occurring below  $m/m_0 \approx 0.4$  produced a  $\Delta C_D \approx \pm 0.09$  and a yaw amplitude not exceeding  $\pm 0.3^\circ$ . Again, these oscillations might result from separation on the nose at reduced mass flows, as indicated in reference 6 for an annular inlet with NACA 1-80-100 inlet lips and a centerbody of fineness ratio 3.0.

#### External-Drag Coefficient

The external-drag coefficient as a function of Mach number is presented for several mass-flow ratios in figure 9. Because of the slow shutter speed relative to the rate of deceleration of the model, only one drag point at each mass-flow ratio was obtained on the steep portion of the drag rise. The curves were faired in this region by assuming the slope to be independent of mass-flow ratio, and the shallowest slope consistent with the data points at either end of the steep portion of the curve was used. Thus the values of external-drag coefficient shown between Mach numbers of 0.94 to 1.03 are largely dependent on the manner of fairing used. Also shown is the total drag coefficient minus base-drag coefficient, corrected for wind effects, for the parabolic body of revolution of reference 1.

The drag coefficients at mass-flow ratios of 0.8 and 0.9 were essentially the same throughout the Mach number range (fig. 9). The drag coefficient at these mass-flow ratios varied from approximately 0.12 at  $M_0 = 0.8$  to a nearly constant value of about 0.35 at  $M > 1.05$ . The drag coefficient of 0.35 at supersonic speeds is quite high in comparison with the drag of the body of revolution from reference 1.

The reason for this high drag rise can be indicated by considering the axial distribution of cross-sectional area normal to the airstream. Reference 7 shows that the zero-lift drag rise of a body is primarily dependent on this axial area distribution. Figure 10 presents a dimensionless plot of cross-sectional area as a function of body length for both the present model and the parabolic body of revolution reported in reference 1. The fin area which was identical for both models has been neglected. The canopy and wheel-well fairing of the present model begin at  $X/L = 0.155$ . The inlet station is  $X/L = 0.25$ . Although the effect of the vertical rise in the area curve caused by the inlets is not known at present, it would be expected to be small at maximum flow rates.

The presence of the canopy and wheel-well fairing on the forebody steepens the slope of the area curve ahead of the inlet station as compared to the parabolic body. The relative bluntness of the inlet lips contributes to the initial rapid increase in area just behind the inlets, while the canopy causes a more forward location of the maximum area station, followed by a relative sharp decrease in area to  $X/L = 0.42$ . As

indicated in reference 7, these steeper slopes result in increasing the transonic drag rise of the present model over that of the parabolic body. The data of reference 8 indicate that the reduction in nose fineness ratio caused by the more forward location of the maximum area station of the inlet model would result in appreciably higher supersonic drag for the inlet model than for the parabolic body. Therefore, the region between  $X/L = 0.25$  and  $X/L = 0.42$  (exclusive of the inlet area itself) would be expected to be especially costly in increasing the drag rise since the corresponding region of the parabolic body contributes very little to the forebody pressure drag at transonic speeds.

The variation of external-drag coefficient with mass-flow ratios is shown in figure 11 for several Mach numbers. Throughout the Mach number range, the effect of decreasing the mass-flow ratio was small until oscillating flow was encountered. As the mass-flow ratio was further decreased, the drag began to rise more abruptly. In the steady-flow region, however, the penalty in drag for spillage was small.

#### Total-Pressure Recovery

Total-pressure recovery after diffusion as a function of Mach number is presented in figure 12 for several mass-flow ratios. At subsonic speeds, maximum recovery was obtained at  $m/m_{\infty} = 0.8$ , whereas above  $M_{\infty} = 1.2$  the maximum recovery was obtained at  $m/m_{\infty} = 0.9$ . At  $M_{\infty} = 0.8$  the maximum recovery was 0.92, and it decreased with increasing Mach number until, at  $M_{\infty} = 1.45$ , it was 0.77, about 18 percent less than free-stream normal-shock recovery. The recoveries presented herein are about 3 percent lower than recoveries measured in flight tests of an airplane employing this inlet configuration but with different internal geometry. The airplane was tested up to a Mach number of 1.0 for mass-flow ratios between 0.65 and 0.85 (ref. 9).

The total-pressure recovery after diffusion is plotted in figure 13 against mass-flow ratio for several Mach numbers as determined from the flight test using nose A. Also shown are the data obtained from the preflight tests at  $M_{\infty} = 1.55$  for the three nose shapes tested. (See table I.) Choking at the throat rake supports limited the maximum mass-flow ratio obtained in the preflight tests to a lower value than was obtained in flight. At  $M_{\infty} = 1.55$  and for the mass-flow range of the preflight tests, oscillating flow was obtained with all three nose shapes.

The total-pressure recovery obtained with nose A during the preflight tests agreed favorably with the total-pressure recovery measured in flight. The total-pressure recovery obtained with nose B was 0.09 to 0.11 less than the recovery with nose A. The recovery with nose C was 0.03 to 0.06 less than the recovery with nose A.

Figure 14 presents the total-pressure profiles measured at the right-inlet minimum-area station during preflight tests. Profiles are presented for nose A for three mass-flow ratios at  $M_\infty = 1.55$  and for one mass-flow ratio at  $M_\infty \approx 0.7$ . Similar total-pressure profiles were obtained with noses B and C. The flagged symbols show the two total pressures measured in the left inlet. The static pressures obtained in each inlet are shown as horizontal lines. The mass-flow ratios and total-pressure recoveries after diffusion were determined from throat measurements in the left duct and are shown for reference in figure 14.

The profile shapes show that a thick boundary layer and, in some cases, separated flow, entered the inlet at  $M_\infty = 1.55$ . In general, the total pressure at the inlet decreased with decreasing mass flow. It appears that a large percentage of the losses measured after diffusion occurred prior to the inlet as indicated in figure 14. The two total-pressure measurements in the left inlet showed fair agreement with the corresponding tubes in the right inlet, and the static pressures obtained in the two inlets were in good agreement.

The inlet total-pressure profiles presented at the extreme right of figure 14 were obtained during a preflight test at  $M_\infty \approx 0.7$ . Steady flow was obtained and the three rakes gave almost identical profiles. The recovery at the inlet was about 0.97, whereas the recovery after diffusion was 0.94. It can be concluded then that, at subsonic speeds at the higher flow rates, the flow at the inlet was reasonably uniform and the diffuser losses were small. The diffuser losses for the steady flow region would be expected to be of this order of magnitude.

The maximum total-pressure recovery after diffusion obtained with the twin side inlet of the present tests is compared with several annular and somewhat similar scoop inlets in figure 15. Data from reference 5 are presented for two annular inlets with ogival innerbodies, 5 and 2.5 diameters long, respectively. Data of reference 6 are presented for a twin side inlet with a  $19^\circ$  conical innerbody 3 diameters long. Also shown are data for an annular inlet with a  $15^\circ$  ramp (ref. 10) and two twin-scoop inlets enclosing 61.5 percent of the maximum forebody circumference (ref. 11), all having forebodies 5 diameters long. (The present inlet enclosed approximately 52 percent of the forebody circumference.) All of the data presented are for tests made without boundary-layer removal.

The data of reference 6 show that a slight improvement in recovery can be achieved in the lower Mach number range by using a conical innerbody instead of a curved profile. At the higher Mach numbers, however, the data of references 5, 10, and 11 indicate the poor recovery obtained during the present tests as compared to the recovery of a nose inlet

was typical of this type of inlet without boundary-layer control. Furthermore, all inlets were subject to flow instability over a wide range of mass-flow ratios (in general, for mass-flow ratios less than 0.7).

In general, these data indicate that, to obtain high recoveries at Mach numbers in excess of 1.0 with annular-type inlets having inner-bodies 3 diameters long or longer, some provision for boundary-layer removal must be provided. Without such a provision, this inlet type is inherently subject to poor recovery and instability.

#### CONCLUSIONS

Results of flight and preflight tests of a twin side-inlet model including a pilot's canopy and wheel-well fairing indicated the following:

1. Oscillating flow was encountered throughout the Mach number range. The maximum mass-flow ratio at which this oscillating flow occurred varied from approximately 0.63 at a free-stream Mach number of 0.80 to about 0.81 at a free-stream Mach number of 1.45.
2. The amplitude of the oscillations amounted to an increment in the total-drag coefficient of  $\pm 0.10$  at Mach numbers greater than 1.1 and as much as  $\pm 0.09$  at Mach numbers less than 0.9.
3. At supersonic speeds, the minimum external-drag coefficient was about 0.35, a value considerably higher than that obtained with a body of revolution of the same fineness ratio.
4. Throughout the Mach number range the increase in external-drag coefficient with decreasing mass-flow ratio did not exceed 0.01 in the region of steady flow.
5. The maximum total-pressure recovery varied from 0.92 at a free-stream Mach number of 0.8 to 0.77 at a free-stream Mach number of 1.45, the latter value being 18 percent less than normal-shock recovery.
6. Two shorter nose shapes tested at a free-stream Mach number of 1.55 yielded lower total-pressure recoveries than were obtained with the original nose.

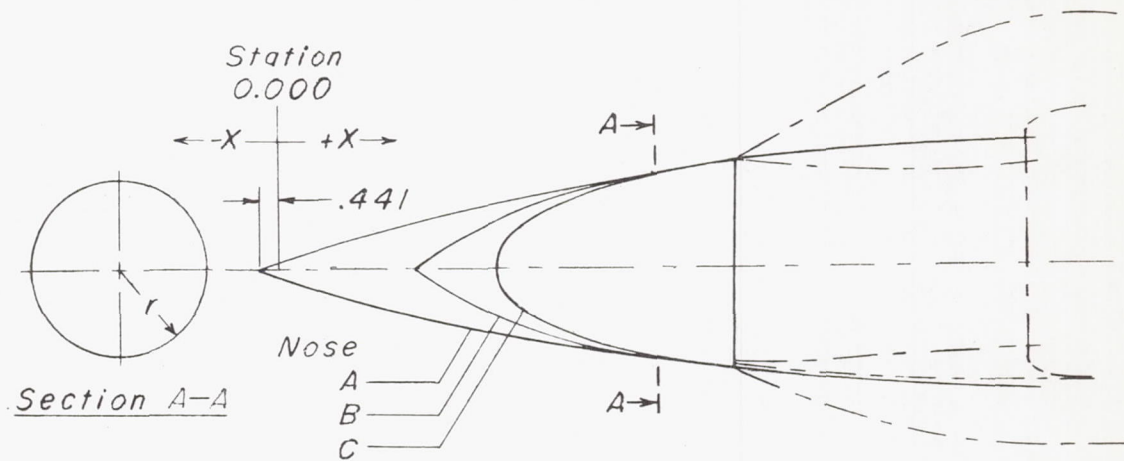
(7) Inlet total-pressure surveys made at a free-stream Mach number of 1.55 indicated the presence of a thick boundary layer and, in some cases, separated flow, at the inlet at all mass flows tested, for all three nose shapes.

Langley Aeronautical Laboratory,  
National Advisory Committee for Aeronautics,  
Langley Field, Va., April 24, 1953.

## REFERENCES

1. Sears, Richard I., and Merlet, C. F.: Flight Determination of the Drag and Pressure Recovery of an NACA 1-40-250 Nose Inlet at Mach Numbers From 0.9 to 1.8. NACA RM L50L18, 1951.
2. Bohm, H., and Koppe, M.: The Influence of Friction on Steady Diffuser Flows at High Speed. B.I.G.S. - 47, Joint Intelligence Objectives Agency, Washington, D. C., July 23, 1946.
3. Martin, Norman J., and Holzhauser, Curt A.: Analysis of Factors Influencing the Stability Characteristics of Symmetrical Twin-Intake Air-Induction Systems. NACA TN 2049, 1950.
4. Faget, Maxime A., Watson, Raymond S., and Bartlett, Walter A., Jr.: Free-Jet Tests of a 6.5-Inch-Diameter Ram-Jet Engine at Mach Numbers of 1.81 and 2.00. NACA RM L50L06, 1951.
5. Davis, Wallace F., Brajnikoff, George B., Goldstein, David L., and Spiegel, Joseph M.: An Experimental Investigation at Supersonic Speeds of Annular Duct Inlets Situated in a Region of Appreciable Boundary Layer. NACA RM A7G15, 1947.
6. Pendley, Robert E., Robinson, Harold L., and Williams, Claude V.: An Investigation of Three Transonic Fuselage Air Inlets at Mach Numbers From 0.4 to 0.94 and at a Mach Number of 1.19. NACA RM L50H24, 1950.
7. Whitcomb, Richard T.: A Study of the Zero-Lift Drag-Rise Characteristics of Wing-Body Combinations Near the Speed of Sound. NACA RM L52H08, 1952.
8. Hart, Roger G., and Katz, Ellis R.: Flight Investigations at High-Subsonic, Transonic, and Supersonic Speeds To Determine Zero-Lift Drag of Fin-Stabilized Bodies of Revolution Having Fineness Ratios of 12.5, 8.91, and 6.04 and Varying Positions of Maximum Diameter. NACA RM L9I30, 1949.
9. Sohn, R. F., Grose, G. G., Allen, D. W., Lacey, T. R., and Gillooly, R. P.: Model XF3H-1 Analysis of Preliminary Flight Test Results. Rep. No. 2496, McDonnell Aircraft Corp., Feb. 27, 1952.
10. Brajnikoff, George B.: Pressure Recovery at Supersonic Speeds Through Annular Duct Inlets Situated in a Region of Appreciable Boundary Layer. II - Effect of an Oblique Shock Wave Immediately Ahead of the Inlet. NACA RM A8F08, 1948.
11. Davis, Wallace F., and Goldstein, David L.: Experimental Investigation at Supersonic Speeds of Twin-Scoop Duct Inlets of Equal Area. I.- An Inlet Enclosing 61.5 Percent of the Maximum Circumference of the Forebody. NACA RM A7J27, 1948.

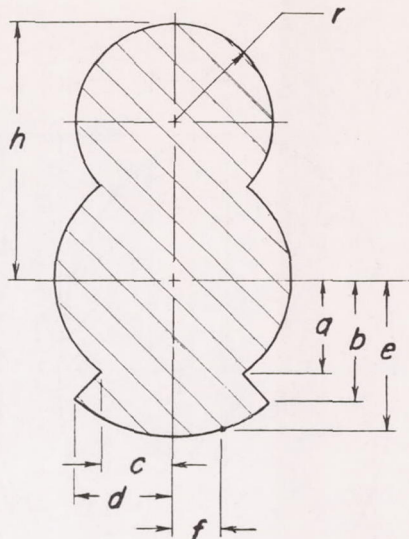
TABLE I.- NOSE DESIGN COORDINATES



| Nose A |        | Nose B |        | Nose C |        |
|--------|--------|--------|--------|--------|--------|
| X      | r      | X      | r      | X      | r      |
| -0.441 | 0.000  | 4.292  | 0.000  | 5.439  | 0.000  |
| -0.110 | 0.104  | 4.704  | 0.332  | 5.585  | 0.538  |
| 1.029  | 0.448  | 5.439  | 0.859  | 5.880  | 0.905  |
| 2.499  | 0.866  | 6.174  | 1.298  | 6.321  | 1.244  |
| 3.969  | 1.250  | 6.909  | 1.654  | 6.909  | 1.558  |
| 5.439  | 1.602  | 7.644  | 1.938  | 7.644  | 1.851  |
| 6.909  | 1.924  | 8.379  | 2.161  | 8.379  | 2.082  |
| 8.379  | 2.215  | 9.114  | 2.337  | 9.114  | 2.272  |
| 9.849  | 2.475  | 9.849  | 2.476  | 9.849  | 2.434  |
| 12.642 | 2.889  | 11.319 | 2.706  | 11.319 | 2.699  |
|        |        | 12.642 | 2.889  | 12.642 | 2.889  |
| <hr/>  |        |        |        |        |        |
| X      | 14.259 | 15.729 | 17.199 | 18.669 | 20.139 |
| r      | 3.080  | 3.221  | 3.334  | 3.419  | 3.475  |
|        |        |        |        |        | 3.494  |



TABLE II.- CANOPY AND WHEEL-WELL FAIRING DESIGN COORDINATES

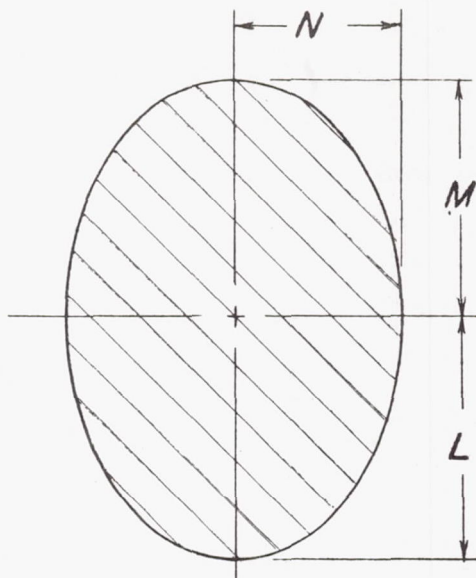


| f    | e             |               |               |               |               |               |               |  |
|------|---------------|---------------|---------------|---------------|---------------|---------------|---------------|--|
|      | Station 14.26 | Station 15.73 | Station 18.67 | Station 21.02 | Station 21.20 | Station 21.51 | Station 21.90 |  |
| 0.00 | 3.61          | 4.15          | 4.89          | 5.14          | 5.14          | 5.14          | 5.15          |  |
| .44  | 3.58          | 4.13          | 4.87          | 5.11          | 5.11          | 5.12          | 5.12          |  |
| .88  | 3.49          | 4.04          | 4.79          | 5.04          | 5.04          | 5.05          | 5.05          |  |
| 1.32 | 3.33          | 3.83          | 4.65          | 4.91          | 4.91          | 4.91          | 4.91          |  |
| 1.76 |               | 3.67          | 4.46          | 4.73          | 4.73          | 4.59          | 4.59          |  |
| 2.21 |               |               | 4.20          | 4.48          | 4.48          | 4.49          | 4.49          |  |
| 2.65 |               |               | 3.85          | 4.16          | 4.16          | 4.17          | 4.17          |  |
| 3.09 |               |               |               | 3.74          | 3.75          | 3.76          | 3.76          |  |

| Station | a    | b    | c    | d    |
|---------|------|------|------|------|
| 12.64   | 2.73 | 2.73 | 0.92 | 0.92 |
| 14.26   | 2.73 | 3.16 | 1.42 | 1.64 |
| 15.73   | 2.67 | 3.33 | 1.81 | 2.25 |
| 18.67   | 2.51 | 3.36 | 2.33 | 3.12 |
| 21.02   | 2.47 | 3.39 | 2.47 | 3.39 |
| 21.20   | 3.30 | 3.40 | 3.28 | 3.40 |
| 21.51   | 3.35 | 3.40 | 3.35 | 3.41 |
| 21.90   | 3.39 | 3.41 | 3.39 | 3.41 |

| Station | h    | r    |
|---------|------|------|
| 12.68   | 2.89 |      |
| 12.94   | 3.06 | 1.01 |
| 12.26   | 3.84 | 1.40 |
| 17.20   | 5.42 | 2.12 |
| 19.26   | 6.29 | 2.46 |
| 21.02   | 6.77 | 2.62 |
| 21.90   | 6.91 | 2.66 |
| 22.79   | 7.00 | 2.69 |
| 24.23   | 7.04 | 2.71 |
| 27.20   | 6.90 | 2.70 |
| 30.14   | 6.60 | 2.62 |
| 33.37   | 6.16 | 2.50 |
| 35.43   | 5.81 |      |

TABLE III.- FUSELAGE PLAN AND PROFILE DESIGN COORDINATES



| Station | L    | M    | N    |
|---------|------|------|------|
| 21.02   | 4.72 | 4.68 | 4.35 |
| 21.20   | 4.91 | 4.81 | 4.44 |
| 21.90   | 5.09 | 4.95 | 4.53 |
| 22.79   | 5.15 | 5.09 | 4.56 |
| 24.23   | 5.15 | 5.29 | 4.56 |
| 27.20   | 5.15 | 5.58 | 4.56 |
| 30.14   | 5.15 | 5.75 | 4.56 |
| 33.37   | 5.15 | 5.81 | 4.56 |
| 38.00   | 5.12 | 5.79 | 4.56 |
| 43.00   | 5.04 | 5.70 | 4.56 |
| 48.00   | 4.93 | 5.51 | 4.56 |
| 52.00   | 4.79 | 5.30 | 4.56 |
| 56.00   | 4.63 | 5.07 | 4.53 |
| 60.00   | 4.44 | 4.80 | 4.40 |
| 64.00   | 4.23 | 4.50 | 4.22 |
| 70.76   | 3.79 | 3.93 | 3.79 |
| 74.67   | 3.49 | 3.59 | 3.49 |
| 80.00   | 3.07 | 3.09 | 3.07 |
| 83.50   | 2.75 | 2.75 | 2.75 |
| 85.00   | 2.60 | 2.60 | 2.60 |

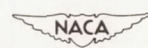
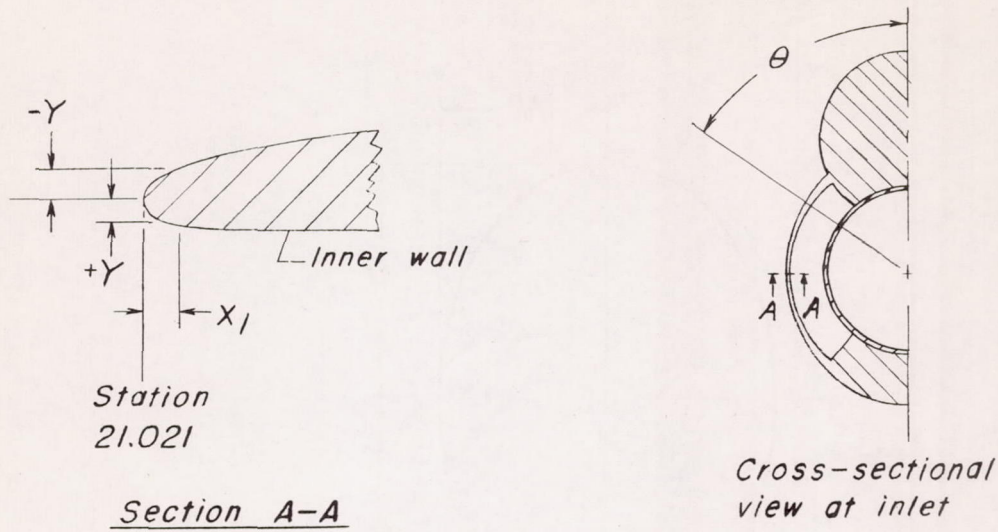


TABLE IV.- INLET LIP DESIGN COORDINATES



| $X_1$ | Lip section coordinates |       |                     |       |                     |       |                      |       |                      |       |
|-------|-------------------------|-------|---------------------|-------|---------------------|-------|----------------------|-------|----------------------|-------|
|       | $\theta = 40^\circ$     |       | $\theta = 60^\circ$ |       | $\theta = 90^\circ$ |       | $\theta = 115^\circ$ |       | $\theta = 135^\circ$ |       |
|       | +Y                      | -Y    | +Y                  | -Y    | +Y                  | -Y    | +Y                   | -Y    | +Y                   | -Y    |
| 0.015 | 0.026                   | 0.035 | 0.024               | 0.028 | 0.022               | 0.026 | 0.024                | 0.029 | 0.031                | 0.035 |
| .029  | .034                    | .050  | .031                | .043  | .029                | .038  | .031                 | .044  | .038                 | .050  |
| .074  | .049                    | .082  | .046                | .065  | .043                | .059  | .046                 | .068  | .056                 | .085  |
| .118  | .056                    | .103  | .054                | .082  | .050                | .074  | .054                 | .084  | .065                 | .107  |
| .176  | .059                    | .126  | .056                | .101  | .051                | .088  | .056                 | .103  | .066                 | .131  |
| .294  |                         | .162  |                     | .129  |                     | .113  |                      | .134  |                      | .166  |
| .441  |                         | .190  |                     | .153  |                     | .135  |                      | .157  |                      | .196  |
| .588  |                         | .215  |                     | .173  |                     | .153  |                      | .176  |                      | .222  |
| .882  |                         | .248  |                     | .200  |                     | .178  |                      | .204  |                      | .257  |
| 1.176 |                         | .269  |                     | .218  |                     | .194  |                      | .222  |                      | .279  |

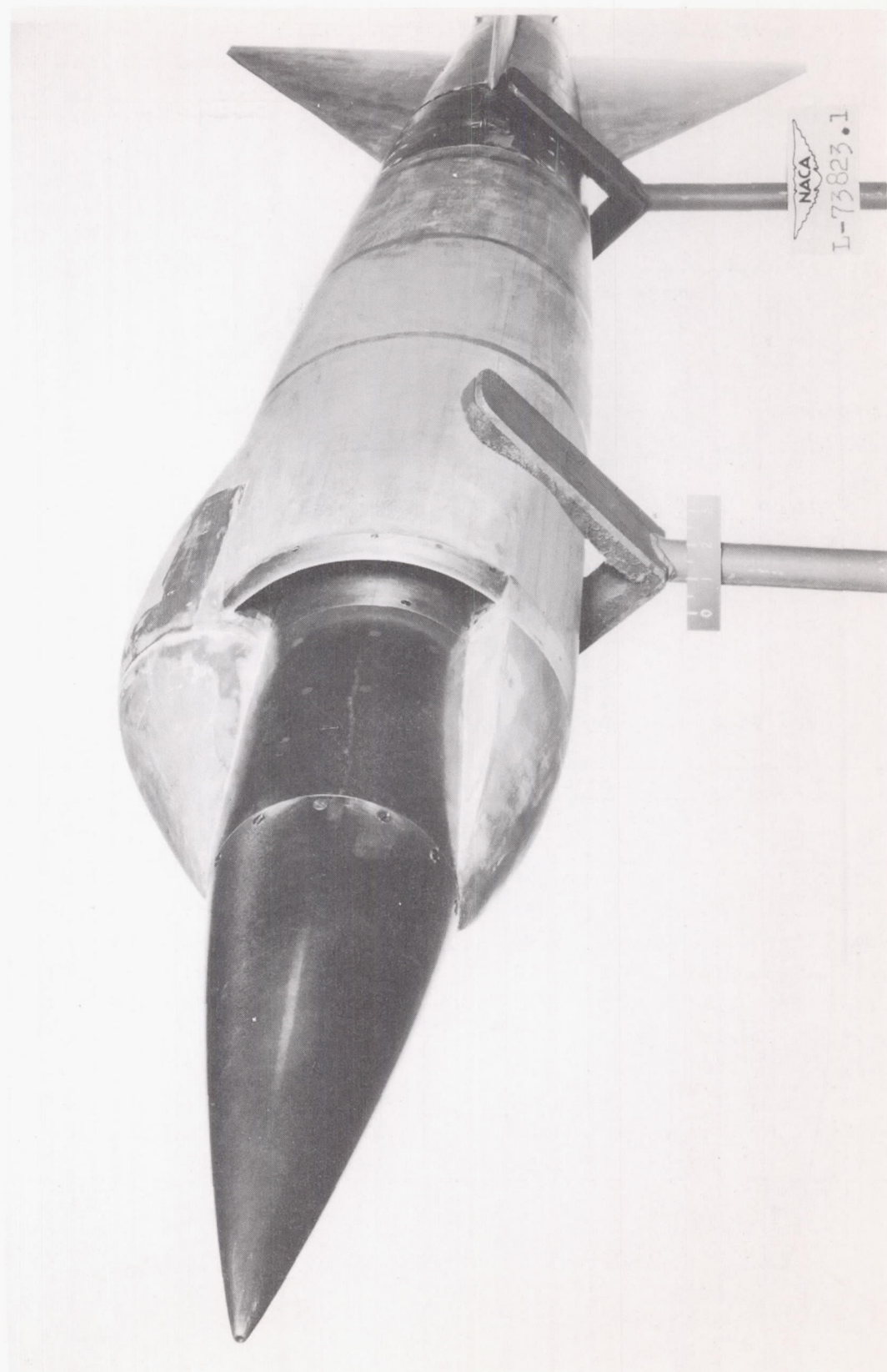


Figure 1.- Photograph of the model.

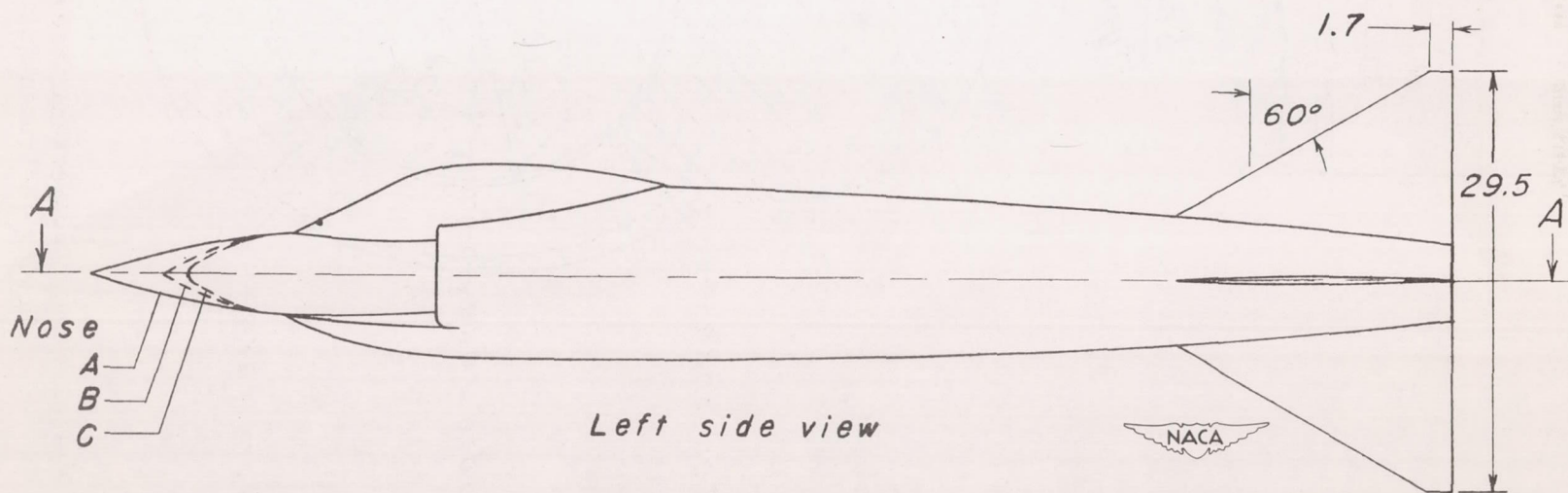
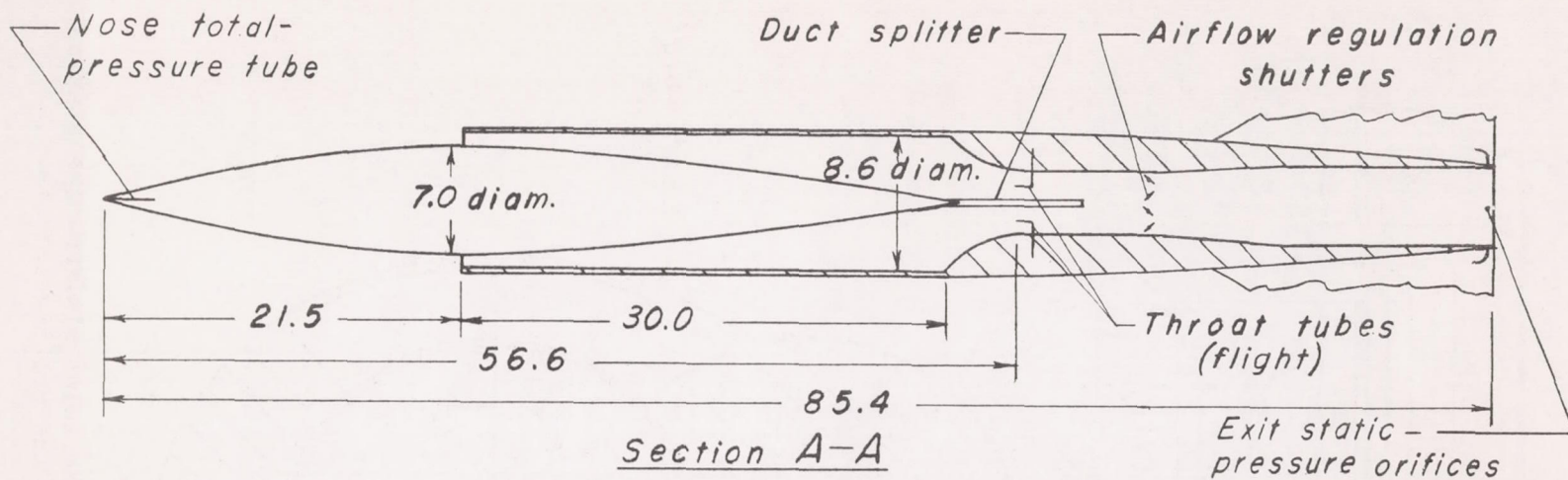


Figure 2.- Drawing of the model. All dimensions are in inches.

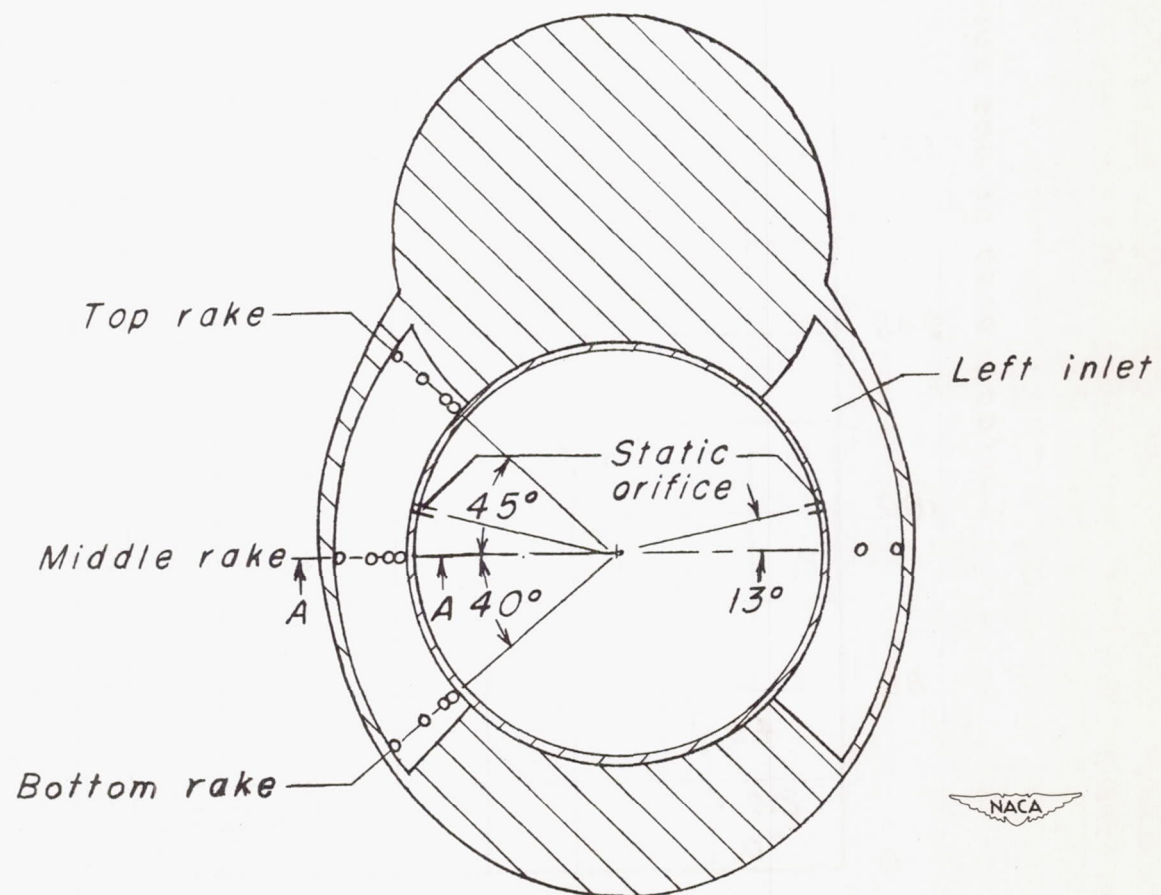
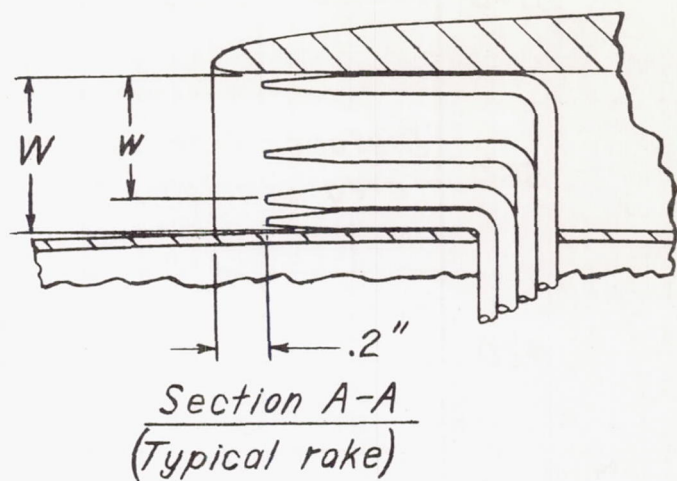


Figure 3.- Cross-sectional view at the inlet minimum-area station, showing instrumentation for the preflight tests.

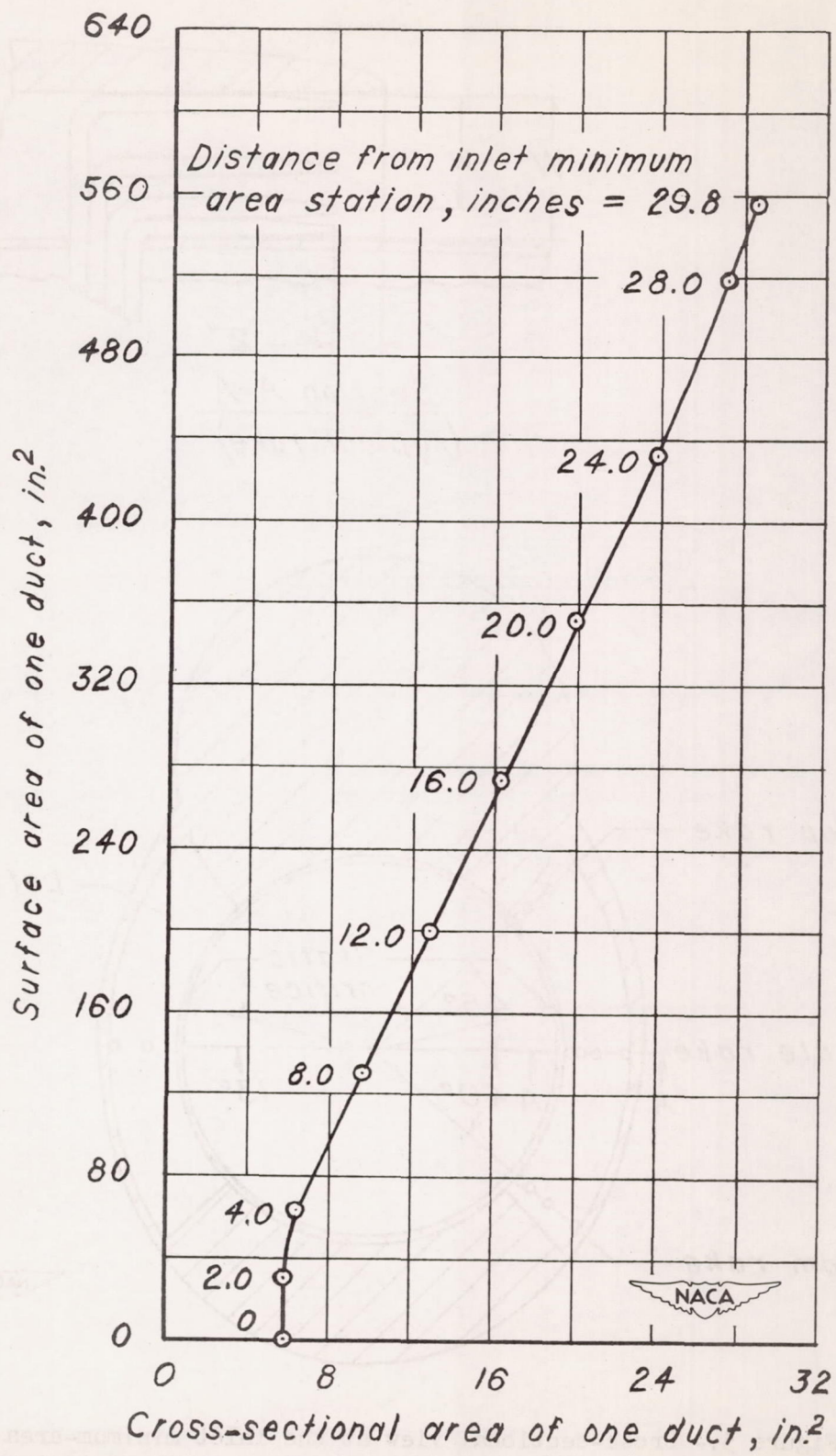
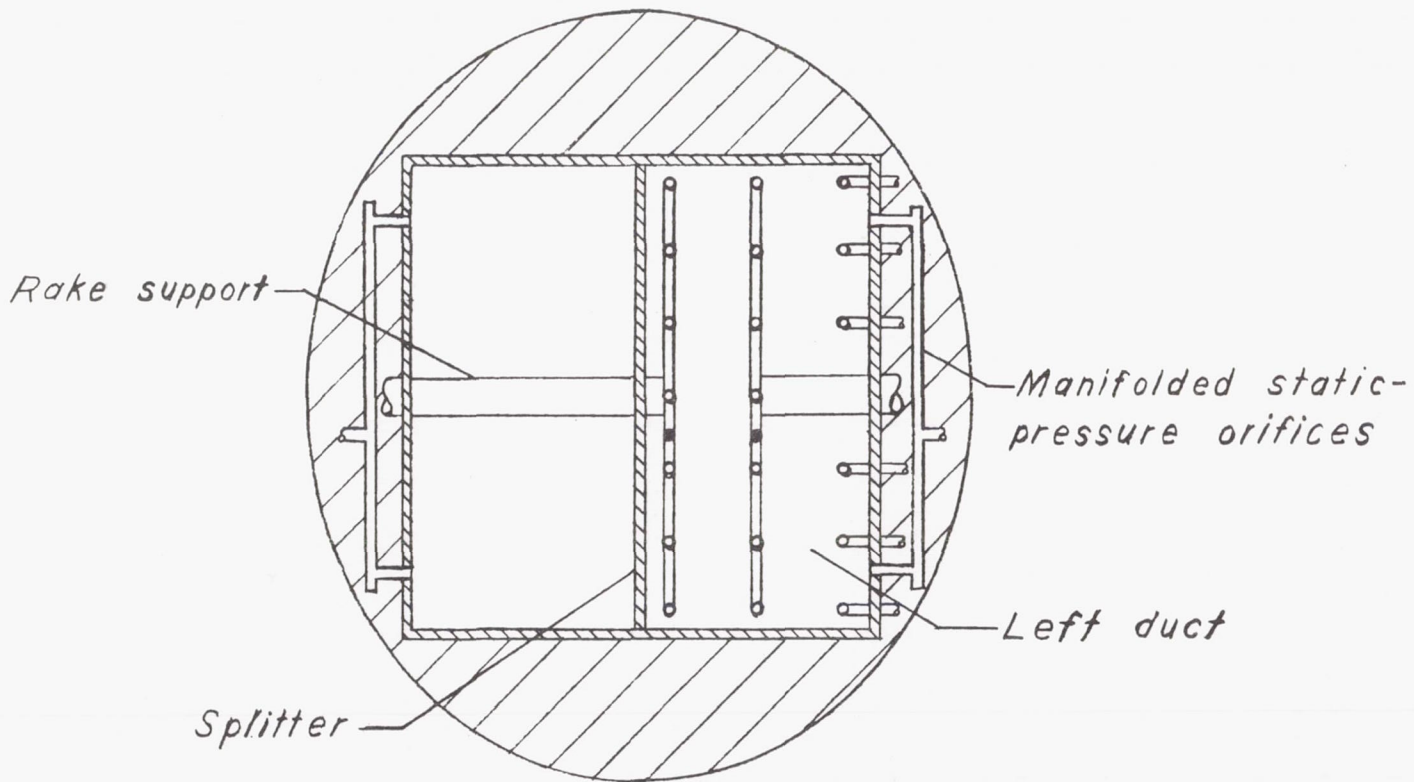


Figure 4.- Variation of diffuser surface area with cross-sectional area.



- Total-pressure tube
- Static-pressure tube

Figure 5.- Cross-sectional view at the throat station, showing instrumentation for the preflight tests.

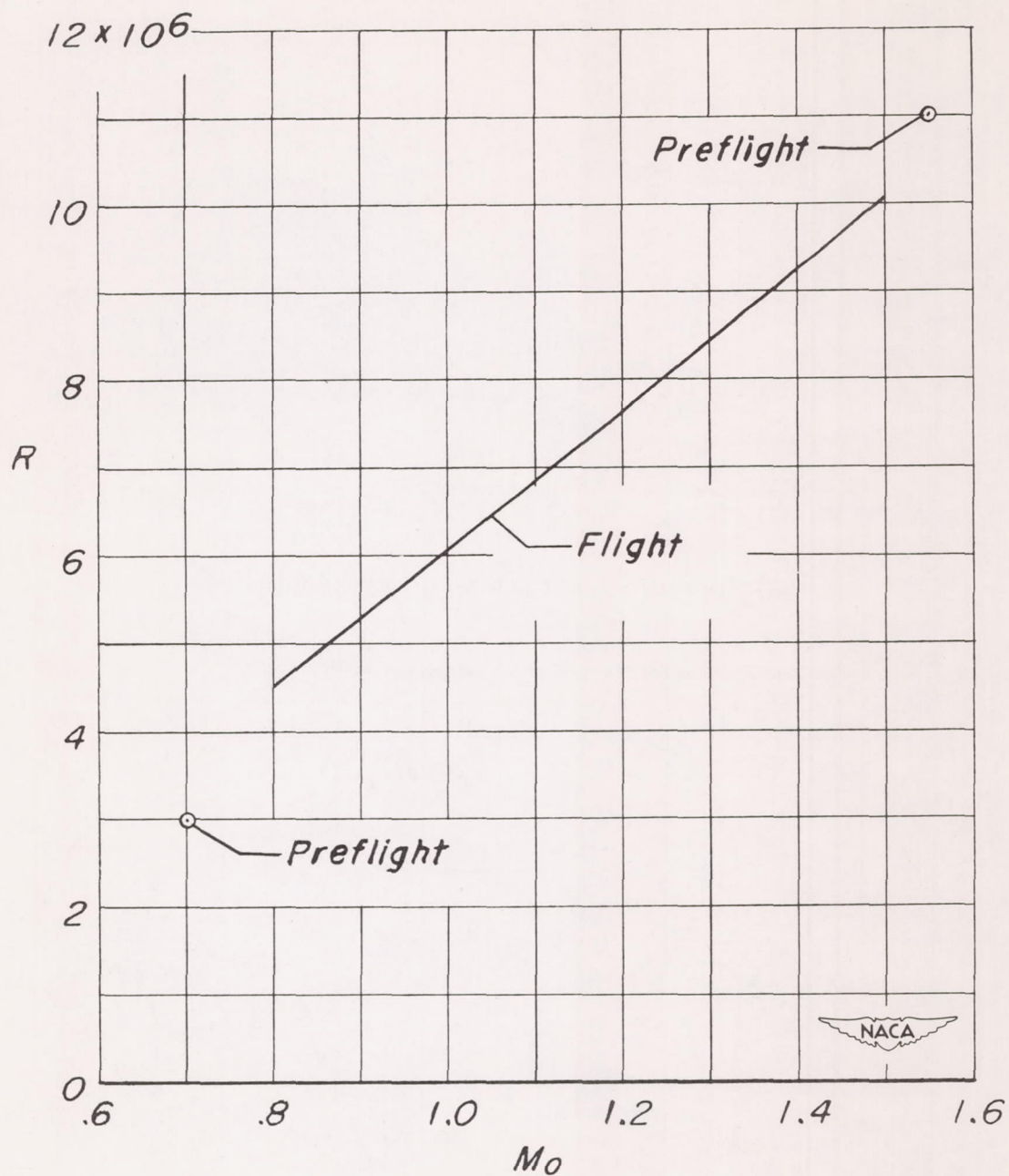
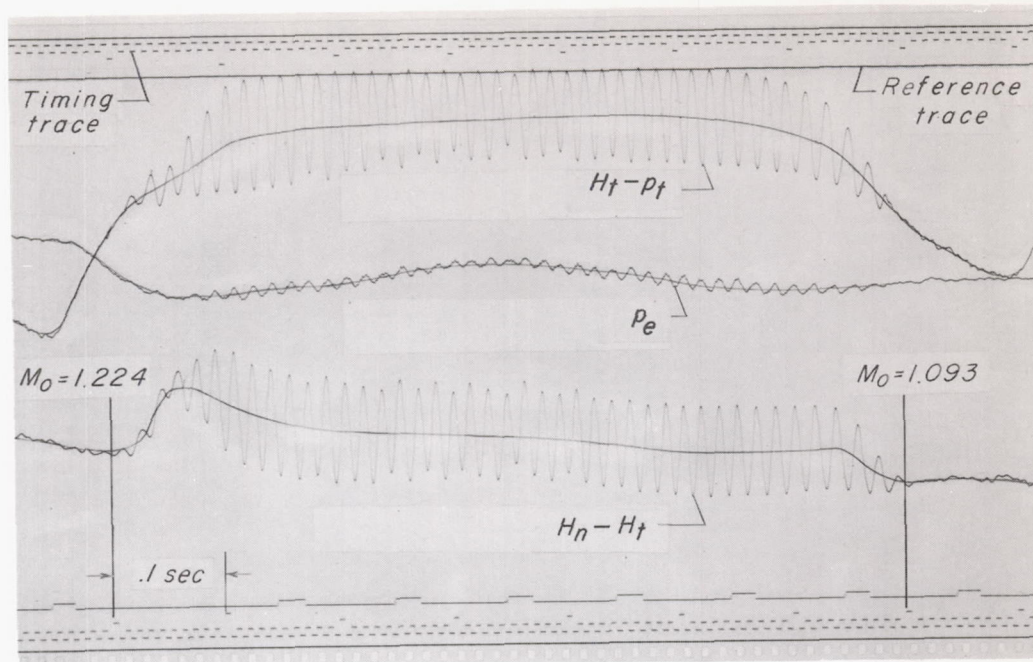
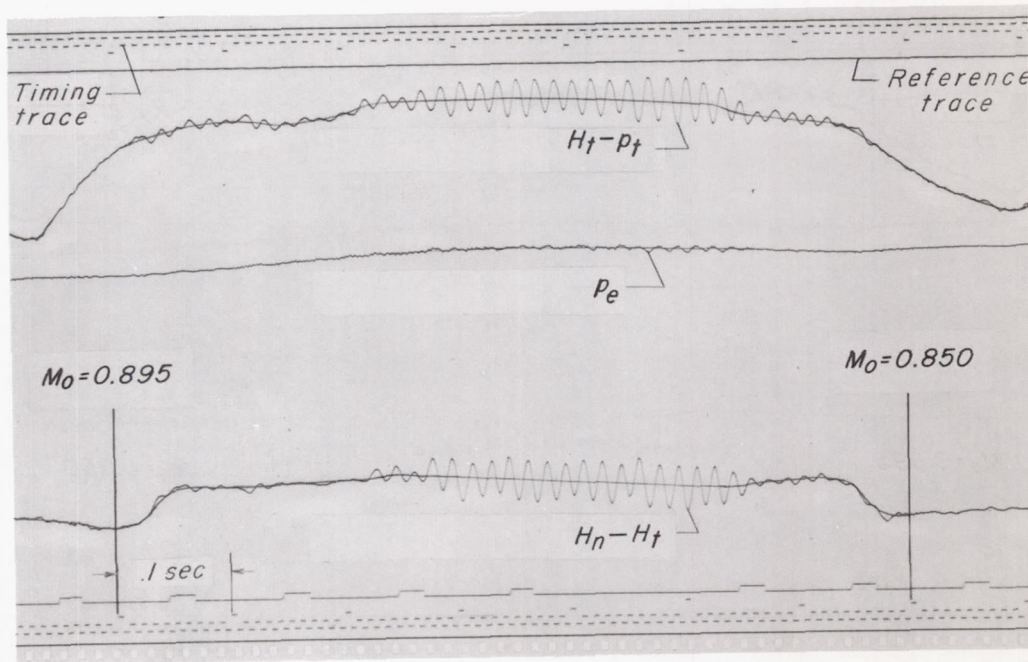


Figure 6.- Reynolds number per foot as a function of Mach number.



(a) Pressure oscillations, supersonic.



(b) Pressure oscillations, subsonic.

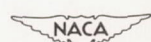
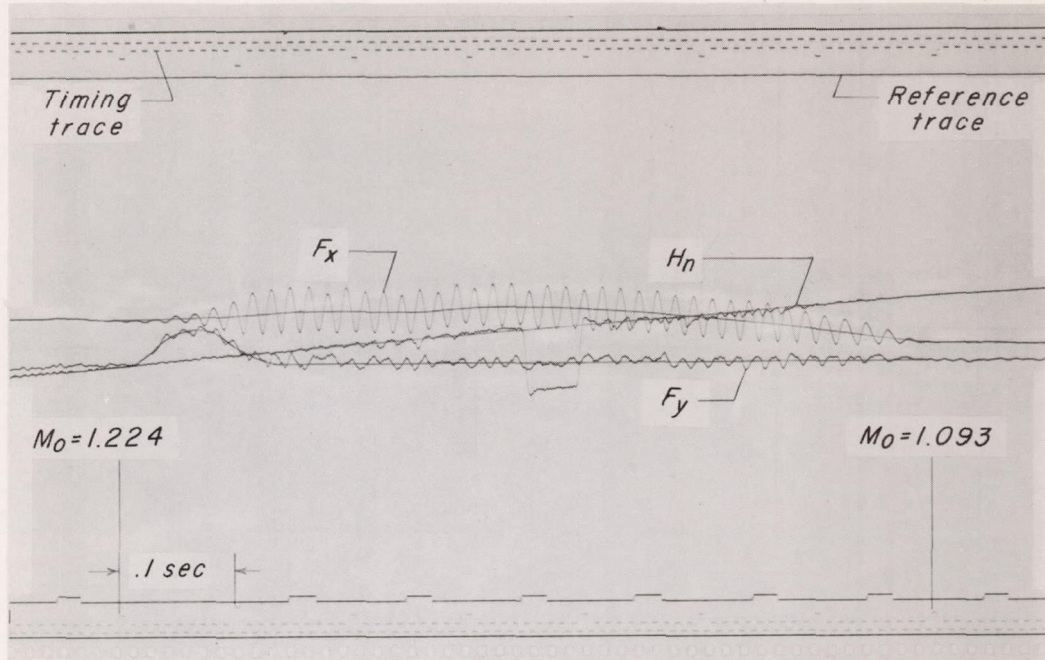
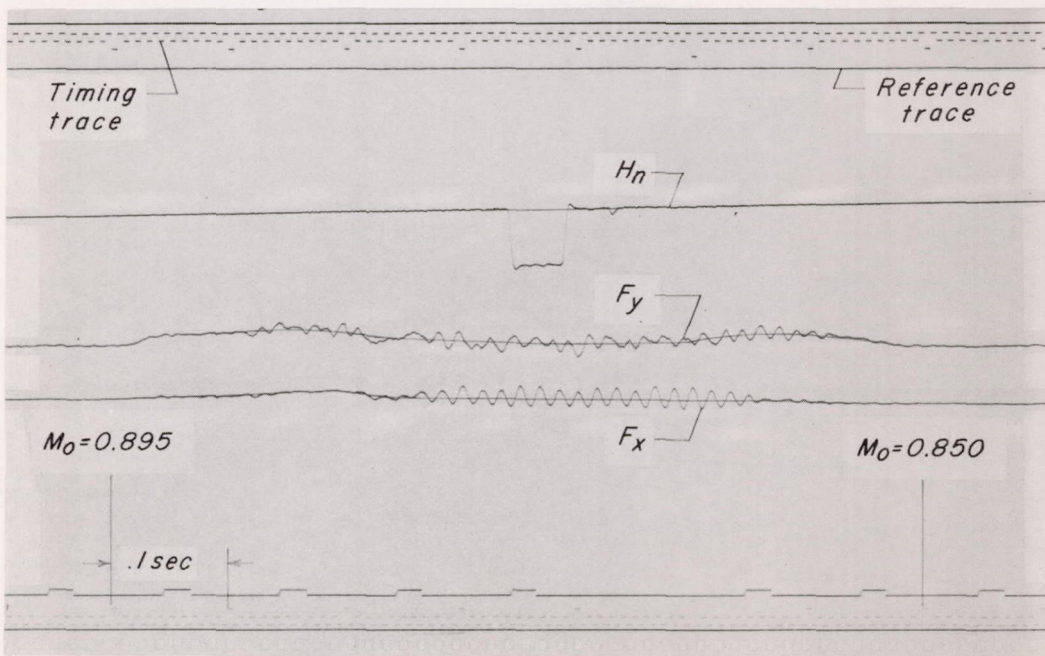


Figure 7.- Portions of the flight telemeter records showing pressure and force oscillations at supersonic and subsonic Mach numbers.

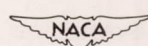


(c) Force oscillations, supersonic.



(d) Force oscillations, subsonic.

Figure 7.- Concluded.



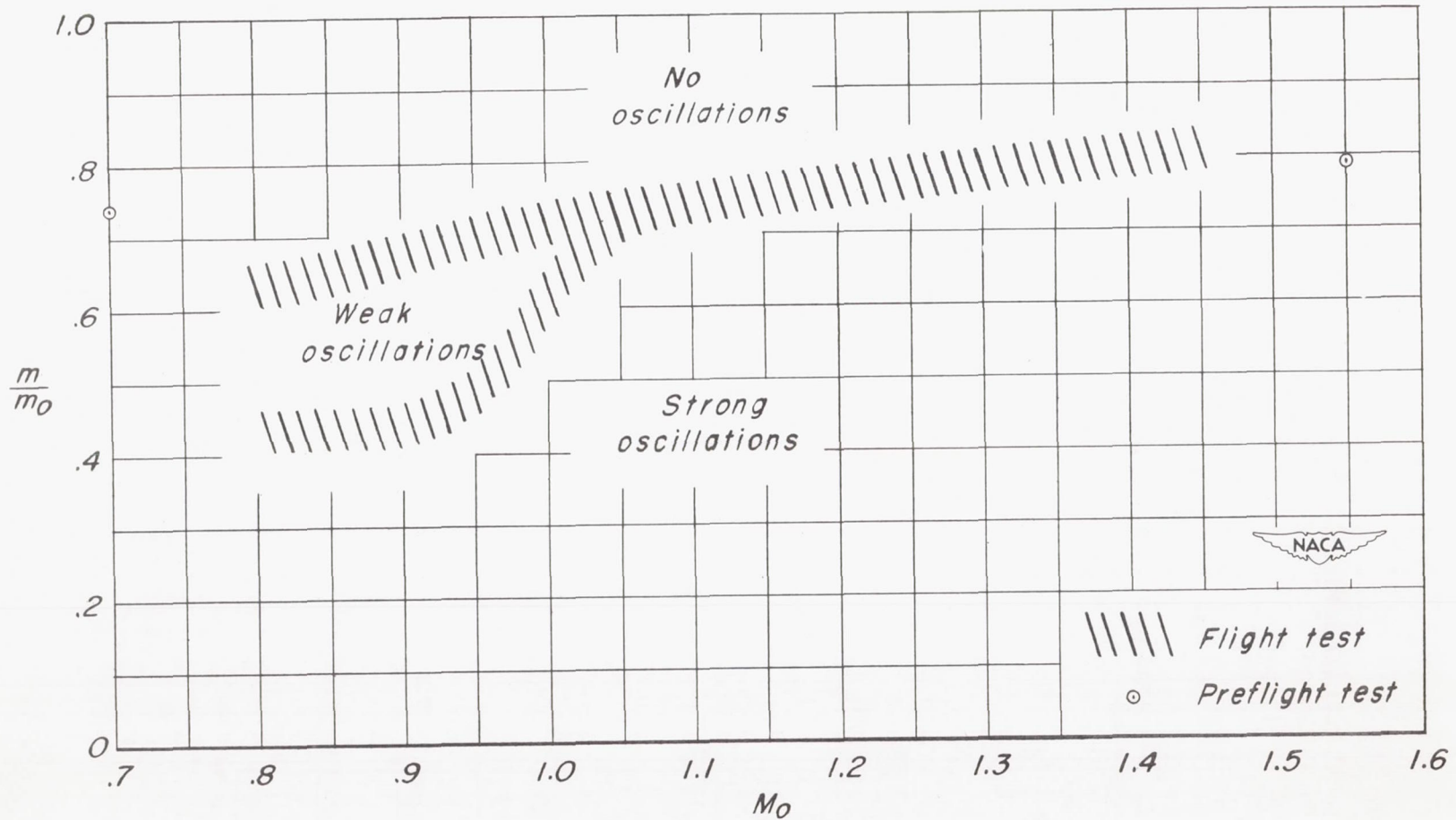


Figure 8.- Mass-flow ratio against Mach number showing regions of oscillating flow.

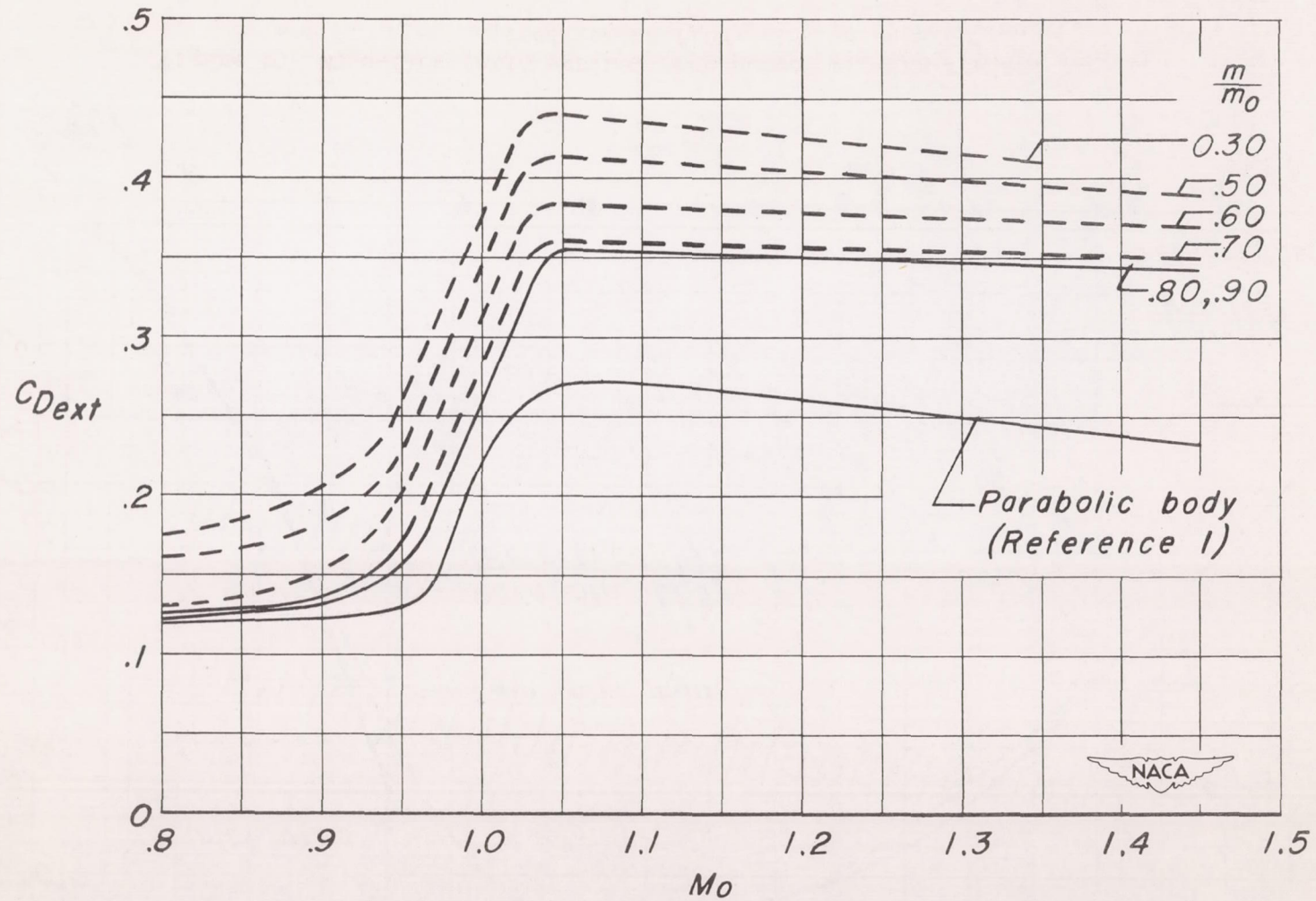


Figure 9.- External-drag coefficient as a function of Mach number for several mass-flow ratios. Curves are dashed in regions of oscillating flow.

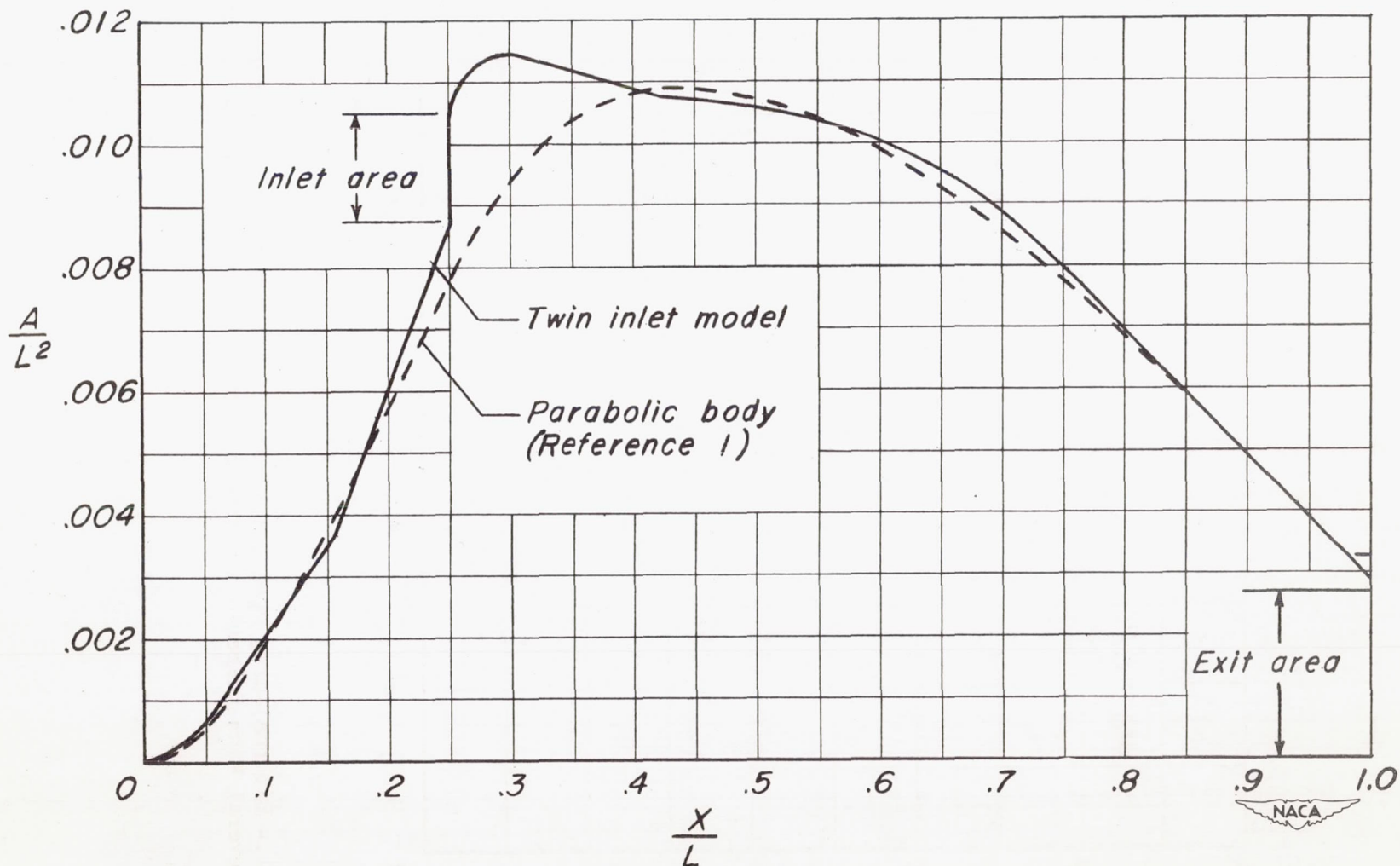


Figure 10.- Comparison of the cross-sectional area distributions of the twin side-inlet model and the parabolic body of reference 1.

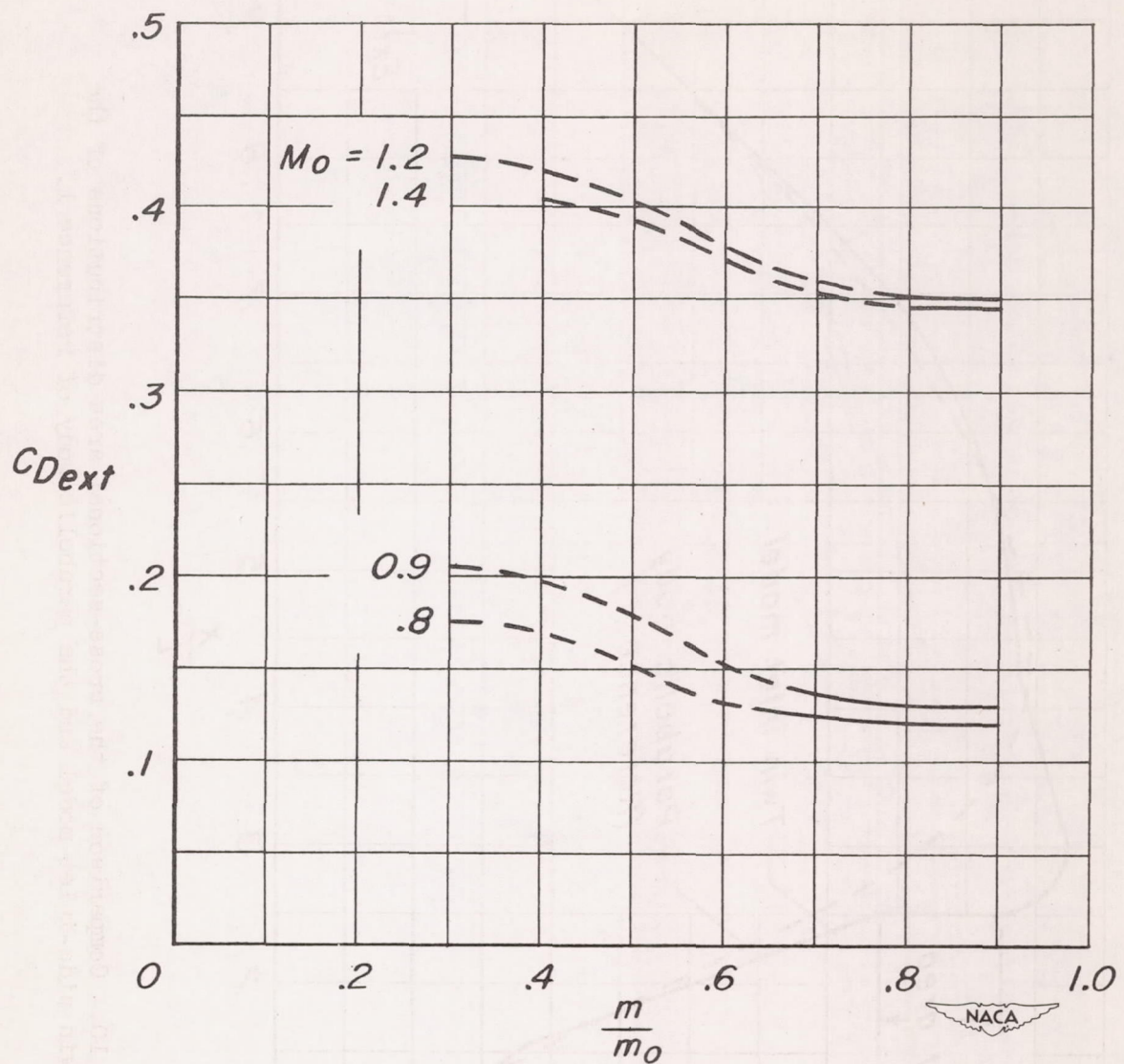


Figure 11.- External-drag coefficient as a function of mass-flow ratio for several Mach numbers. Curves are dashed in regions of oscillating flow.

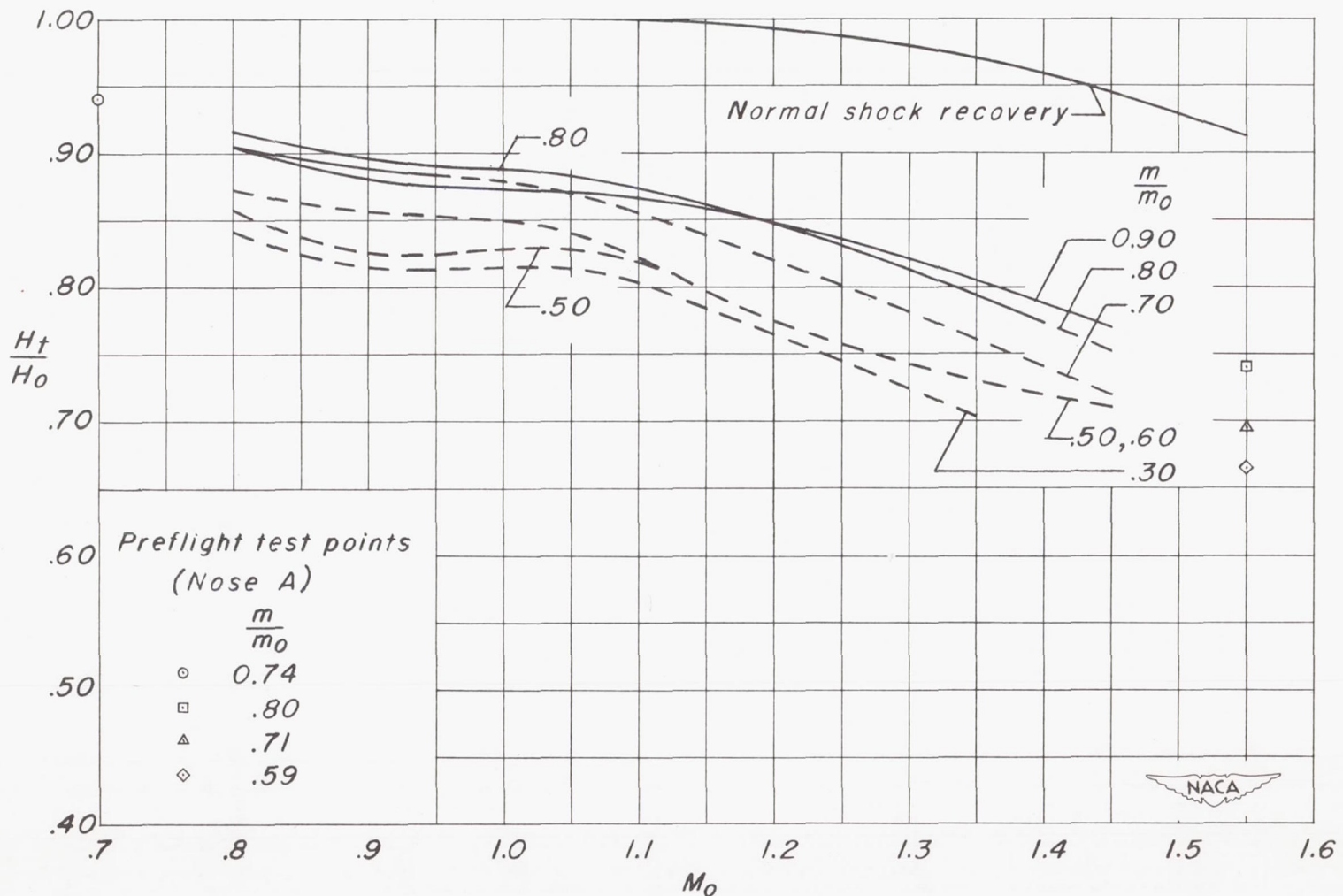


Figure 12.- Total-pressure recovery as a function of Mach number for several mass-flow ratios. Curves are dashed in regions of oscillating flow.

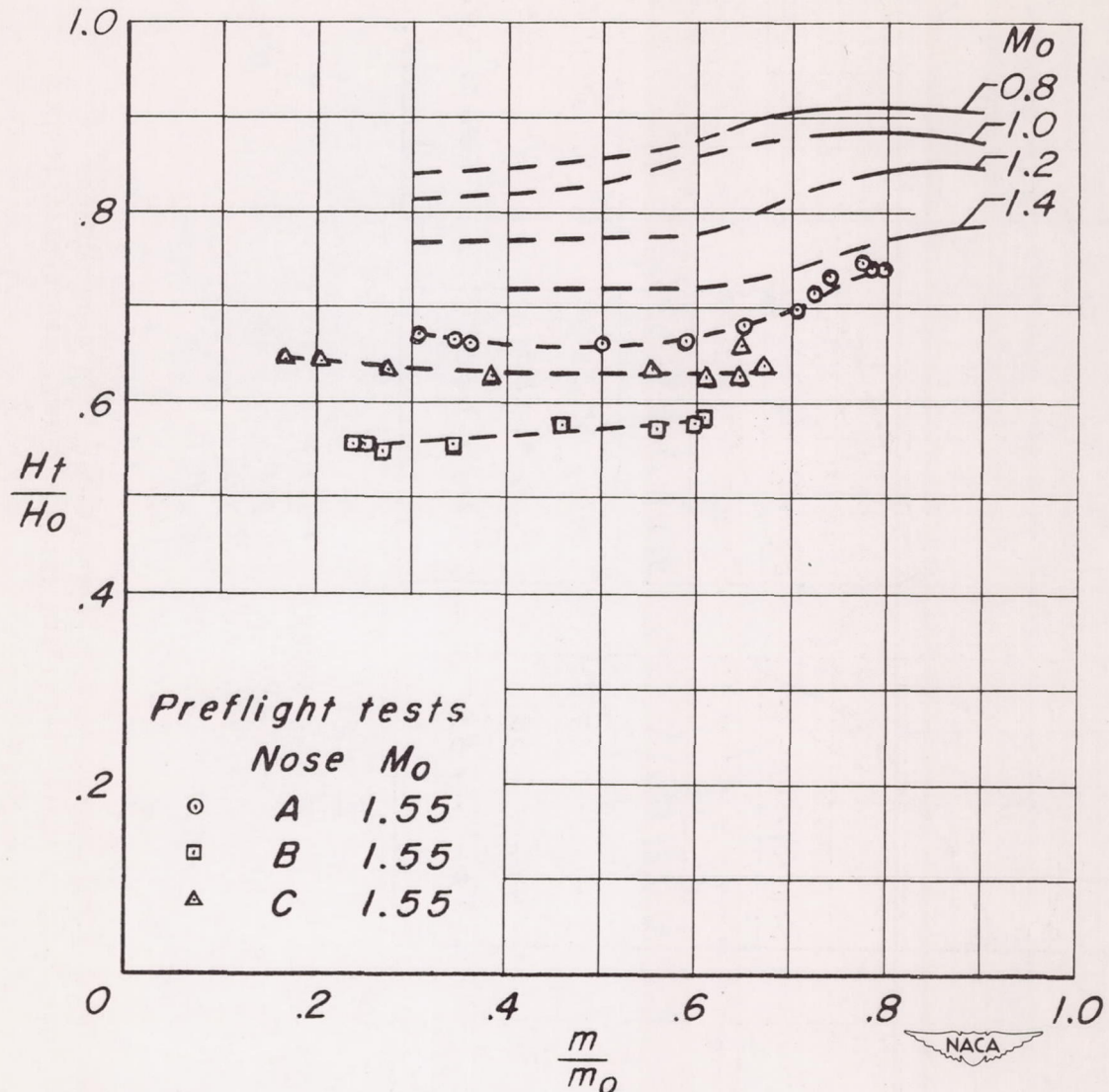


Figure 13.- Total-pressure recovery as a function of mass-flow ratio for several Mach numbers. Curves are dashed in regions of oscillating flow.

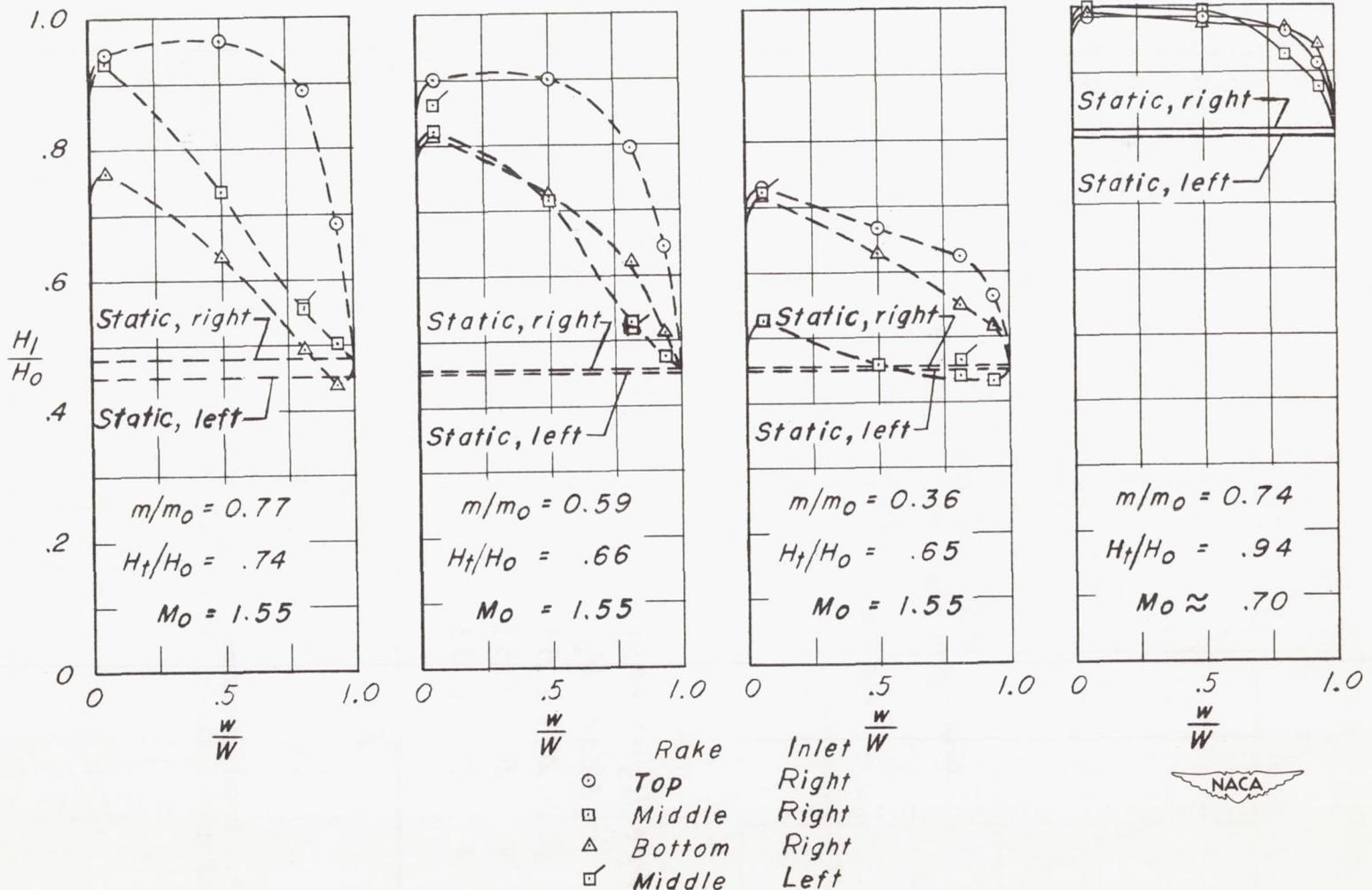


Figure 14.- Total-pressure recovery profiles at the inlet minimum-area station with nose A during preflight tests. Curves are dashed in regions of oscillating flow.

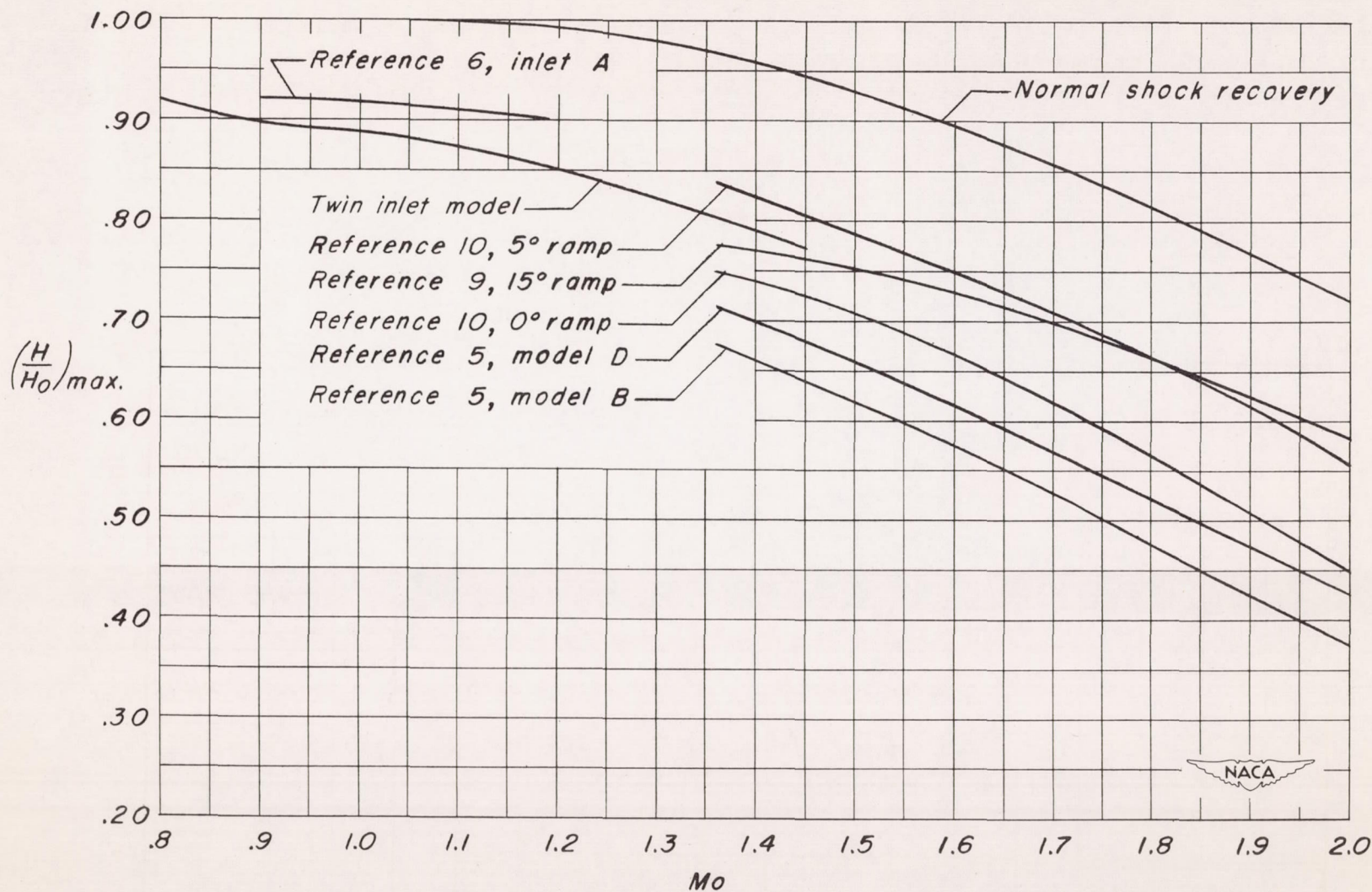


Figure 15.- Comparison of maximum total-pressure recovery of the twin side inlet with several similar inlets.